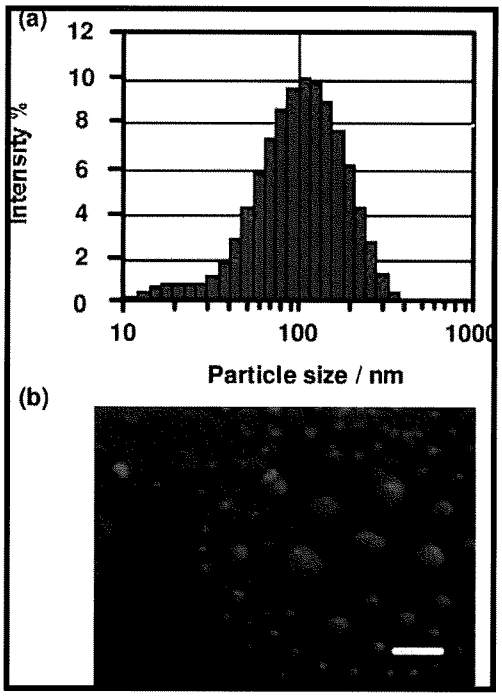

Figure 2. Particle size and morphology of nanoparticles of fluorescein-labeled amphiphilic polysiloxane (Flu-Am-PAPS). (a) Particle size histogram of nanoparticles of Flu-Am-PAPS. The nanoparticles were dispersed in pure water. (b) SEM image of Flu-Am-PAPS. Scale bar: 200 nm.

The nanoparticles had a slightly negative zeta potential (−0.9 mV) in the cell culture medium. The nanoparticle of Am-PAPS dispersed in phosphate buffered saline did not exhibit considerable change in particle size after one week storage at 37 °C (Figure S1a in Supporting Information). Furthermore, particle size measurement using DLS was carried out on the polysiloxane nanoparticles dispersed in cell culture medium containing 5% fetal bovine serum and found that one week storage of polysiloxane nanoparticles in serum containing culture medium at 37 °C caused little change in average particle size and particle size distribution (Figure S1b in Supporting Information). These data suggest that nanoparticles of Am-PAPS are stable in physiological condition. According to our recent report,[15] the NMR spectroscopy for the long alkyl side chains of the amphiphilic polysiloxane indicated that the signal intensity of protons in long alkyl chains become weak when the amphiphilic polysiloxane dissolved in D_2O was measured. Figure 1c shows that the signal observed around δ 1.25 ppm is ascribed to the protons of stearoyl chains attached to Flu-Am-PAPS and the signal intensity of the peak at δ 1.25 ppm of Flu-Am-PAPS dissolved in D_2O is weakened to the 76% of that of the peak at δ 1.25 ppm measured in DMSO (Figure 1d). The decrease in the intensity of the proton signal results from the restricted molecular motion of long alkyl chain and indicates that the molecular aggregation of Flu-Am-PAPS is driven by inter/intra hydrophobic association between stearoyl groups attached to the polysiloxane backbone.

Cellular Uptake of Nanoparticles by Human Aortic Endothelial Cells. Cellular uptake of the nanoparticles by HAECs was observed by fluorescence microscopy. HAECs were cultured for 72 h to obtain confluent culture of HAECs after cell suspension of HAECs was seeded on tissue culture dishes. At 72 h after cell seeding, cell culture medium was replaced with the polymer suspension of Flu-Am-PAPS. Then the HAECs were cultured in the polymer suspension for 15 min, 1, 3, 6, 24, 48, 72, and 144 h to monitor cellular uptake of the nanoparticles of Flu-Am-PAPS. The polymer suspension in cell culture dishes was exchanged daily during the incubation with Flu-Am-PAPS. Clearance of the incorporated nanoparticles from HAECs was observed after the nanoparticle suspension in culture dishes was replaced with EGM-2, growth medium for HAECs. For fluorescence microscopy observation, the cells were rinsed with 37 °C phosphate buffered saline (PBS), then were fixed by immersing into 10% formaldehyde neutral buffer solution at room temperature for 15 min and washed three times with PBS. Fluorescence images of the cells were taken by a fluorescence microscope equipped with a CCD camera at each incubation time. To evaluate cellular uptake of nanoparticles quantitatively, fluorescence intensity (F.I.) per image was determined by integrating the brightness at each pixel of fluorescence image using an image analysis software. The F.I. was normalized in a ratio of the F.I. at each incubation time over the F.I. at 6 h of incubation (the relative fluorescence intensity). The time course of the relative F.I. was plotted on the graph, Figure 3a (closed circles: uptake of nanoparticles; open circles: clearance of nanoparticles). HAECs incorporated progressively nanoparticles of Flu-Am-PAPS until 72 h of incubation and reached saturation thereafter until the end of observation at 144 h of incubation. Decline of F.I. after the removal of Flu-Am-PAPS from the cell culture dishes at 6 h of incubation indicates that the incorporated nanoparticles of Flu-Am-PAPS were gradually excreted from HAECs. However, 40% of the incorporated nanoparticles were still trapped in cytosol of HAECs at 138 h of post incubation (144 h of total incubation time). Meanwhile, the relative F.I. for the uptake dropped to only 2% of the control level (left bar in Figure 3b: 6 h at 37 °C) when HAECs were exposed to the nanoparticles at 4 °C of the incubation temperature for 6 h (middle bar in Figure 3b). Considerable cell detachment was not observed even after 6 h of the incubation at 4 °C. This means that cell culture of HAECs was maintained at a low culture temperature and the HAECs were alive. The temperature triggered dramatic decrease in the relative F.I. suggests that the nanoparticles are mainly incorporated into HAECs by endocytosis, not by adsorption to cell membrane. Endocytosis was restored after the HAECs exposed to low temperature environment were put back to the regular culture condition (cell culture at 37 °C). The reduced relative F.I. corresponding to the nanoparticle uptake at 4 °C increased to 90% of the relative F.I. that was measured after 6 h of incubation with Flu-Am-PAPS nanoparticles at 37 °C (left (incubation at 37 °C for 6 h) and right (incubation at 4 °C for 6 h and postincubation at 37 °C for 6 h) bars in Figure 3b). To ensure that the cellular uptake study was carried out under the condition that the dose of polysiloxane nanoparticles had little toxicity on HAECs, cytotoxicity of the polysiloxane nanoparticles in HAECs was evaluated by colorimetric cell viability assay using WST-8 as an indicator. Cell viability of HAECs was 95% when HAECs were cultured in the growth medium containing 1 mg/mL of Flu-Am-PAPS for 24 h. This suggests that the cellular uptake study was carried out under the condition that the polysiloxane nanoparticles did not exhibit cytotoxicity toward HAECs at 1 mg/mL of Flu-Am-PAPS.

Caveolae as Endocytic Pathway for Nanoparticles. Endocytosis is one of the important cell activities in internalization of various extracellular substances.[20] Endocytic pathways have been taken into account in targeted delivery of drug to vascular tissue. Caveolae are flask-shaped invaginations of cell membrane with diamters of 50−100 nm and are thought to function as

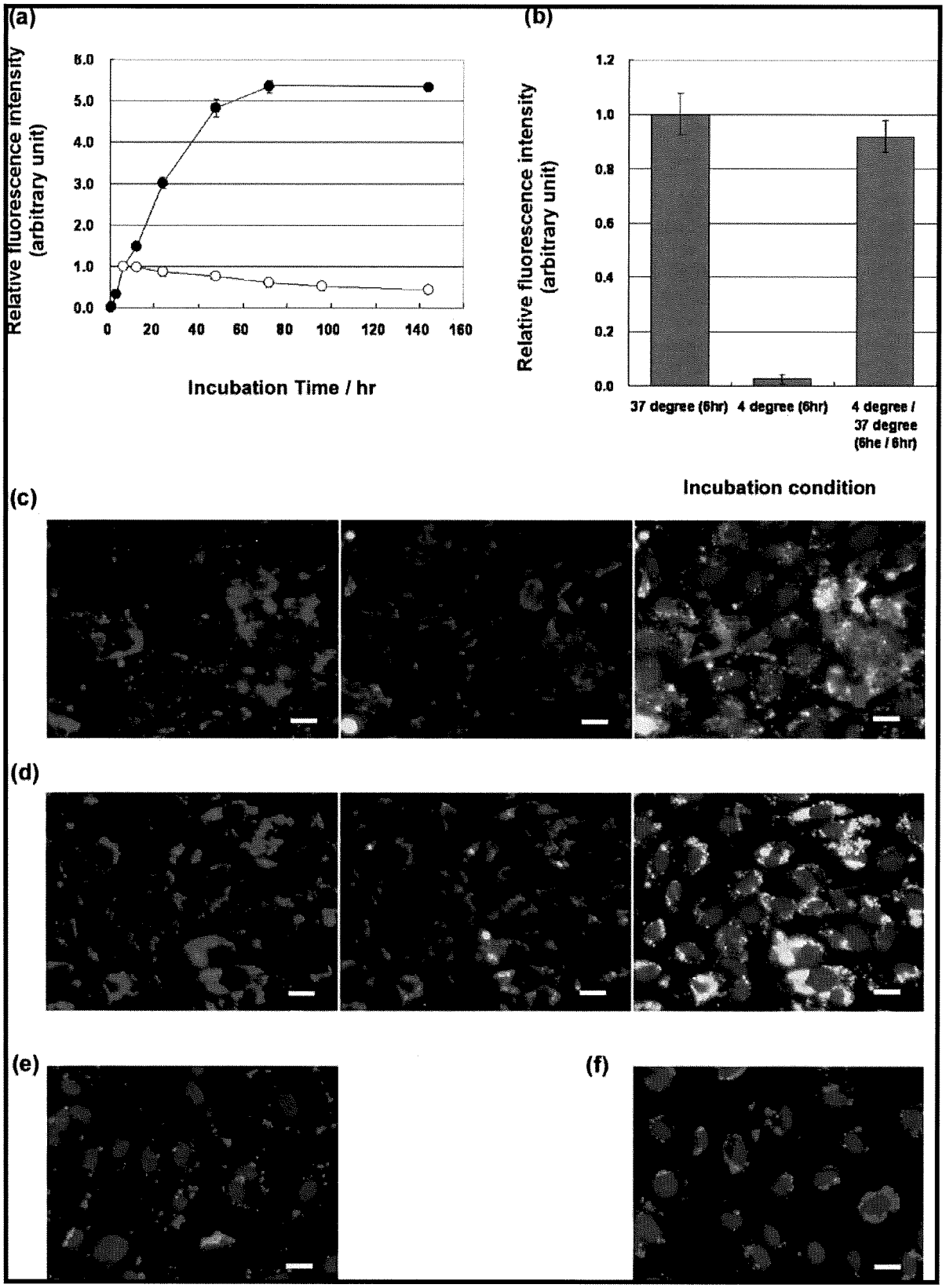

Figure 3. Cellular uptake of fluorescein-labeled amphiphilic polysiloxane (Flu-Am-PAPS). (a) Relative F.I. of Flu-Am-PAPS at each time of incubation with HAECs. The F.I. was measured by integrating brightness at each pixel of fluorescence image and normalized by F.I. at 6 h of incubation. Time course of the cellular uptake of Flu-Am-PAPS by HAECs was represented by closed circles (●). The clearance of the endocytosed Flu-Am-PAPS (○) from HAECs was monitored after HAECs were exposed to the nanoparticles of Flu-Am-PAPS for 6 h and incubated in growth medium. (b) Inhibition and recovery of cellular uptake of Flu-Am-PAPS followed by incubation temperature change (left, 6 h incubation at 37 °C; middle, 6 h incubation at 4 °C; and right, 6 h incubation at 4 °C and then 6 h incubation at 37 °C). Endocytic pathway in HAECs; localization of caveolin-1 and Flu-Am-PAPS in human aortic endothelial cells (HAECs). Caveolin-1 was detected by using primary antibody against caveolin-1 and TRITC-labeled secondary antibody against rabbit. Nucleuses of cells were stained with DAPI. Red: Caveolin-1. Green: Flu-Am-PAPS. Blue: nucleuses. (c) An image taken after 3 h incubation with Flu-Am-PAPS. (d) An image after 24 h incubation with Flu-Am-PAPS. Translocation and accumulation of the nanoparticles of Flu-Am-PAPS were confirmed in HAECs. (e) An image taken after 6 h incubation with Flu-Am-PAPS. (f) An image taken at 18 h of post incubation after the 6 h incubation with Flu-Am-PAPS. Nanoparticles of Flu-Am-PAPS accumulated around the cell nucleus. Scale bar: 20 μm.

platforms for endocytosis and signaling.[21] The caveolae-mediated pathway is prominent and ubiquitous endocytic mechanisms in vascular endothelial cells.[8] Figure 3c and d show fluorescence images of HAECs that incorporated fluorescein-labeled polysiloxane nanoparticles (green) and were immunostained for caveolin-1 (primary antibody against caveolin-1, TRITC-labeled secondary antibody against rabbit; red), which comprises the caveolae. Fluorescence image taken at 3 h of incubation time (Figure 3c) demonstrates that some of the green emissions from nanoparticles (left image in Figure 3c) are overlapped with red emissions from caveolin-1 (middle image in Figure 3c) to make yellow area (right image in Figure 3c). The yellow overlaps suggest that nanoparticles are localized at the caveolae. At 24 h of incubation time, nanoparticles (left image in Figure 3d) were localized as ring-like patterns of overlapped area around nucleuses of HAECs (right image in Figure 3d). This indicates that the nanoparticles of Flu-Am-PAPS were trapped into caveolae in plasma membrane and transported into cytosol of HAECs by 24 h of incubation. The peri-nuclear localization of the nanoparticles (Figure 3f) was also observed when HAECs were exposed to the nanoparticles for 6 h (Figure 3e) and incubated for 18 h after the medium containing nanoparticles was changed to growth medium containing no nanoparticles. The fluorescence imaging data indicate the following process for the uptake of the nanoparticles: (i) the nanoparticles are trapped at caveolae in plasma membrane, (ii) the nanoparticles are internalized into cytosol, and (iii) the nanoparticles are localized at peri-nuclear region. Furthermore, internalization of the nanoparticles into the cytosol of HAECs was confirmed by confocal laser scanning microscopy. The X-Y plane images of HAECs were taken as optical slices with 0.2 μm thick along Z-axis by confocal laser scanning microscope. Figure 4a shows fluorescence intensity profiles of Flu-Am-PAPS along the Z-direction in HAECs. The intensity profiles were obtained by integrating the brightness at each pixel over the whole area of each image, normalizing the intensity to the intensity at basal position (Z = 0 μm) and plotting the normalized intensity as a function of depth in a cell. The intenisty maximum was confirmed in each profile (arrow heads in the graph) and indicates the spatio and temporal position of the nanoparticles in HAECs. Although each profile has two maxima at $Z = 0$ μm and at other position in Z-axis respectively, the intensity maximum that we are discusing here is located above the basal level. The position of the intensity maximum shifted gradually from the apical side (Z = 3 μm) to the basal side (Z = 0−1 μm) of HAECs; Z = 2.4−2.6 μm at 1 h, Z = 1.1−1.9 μm at 3 h, Z = 0.5−1.6 μm at 6 h, and Z = 0.4−1.2 μm at 24 h. Thus, the peak shift clearly shows that the nanoparticles were trapped at the plasma membrane and internalized into the cytosol of HAECs.

The nanoparticles of the amphiphilic polysiloxane can fit into caveolae in the plasma membrane of HAECs, because the histogram of the particle size (Figure 2 (a)) for the nanoparticles of Flu-Am-PAPS indicates that at least 48% of the total population of the nanoparticles have diameters in the range of 10−100 nm, that is comparable to the dimension of caveolae (50−100 nm in both opening diameter and depth). Fluorescence microscope observation demonstrated the colocalization of the nanoparticles and caveolae (Figure 3c and d). To specify the endocytic pathway for the uptake of the nanoparticles we attempted to observe caveolae in HAECs by TEM. Specimens for TEM were prepared by the methods described in the materials and methods after HAECs were incubated with nanoparticles of gold nanoparticle labeled Am-PAPS (Au-Am-PAPS) or Flu-Am-PAPS at 37 °C for 3 h. The nanoparticles (Flu-Am-PAPS) uptaken by HAECs were detected by immunolabeling using anti-fluorescein IgG as a primary antibody and a secondary antibody attached to a gold nanoparticle (diameter: 5 nm). Here we observed TEM specimens by following the two different methods: conventional ultrathin section and rapid-freeze deep-etch immunoreplication.[22] The ultrathin section image (Figure 4b) shows that caveolae (round-shape structures with diameters of about 100 nm: indicated by a square in Figure 4b) are incorporated into cytosol and that dark dots (5−10 nm in diameter) of gold nanoparticles attached to polysiloxane are confirmed in the inner perimeter of caveolae vesicles (indicated by arrows in the inset of Figure 4b). Figure 4c shows the ultrathin section image of cytosol of the intact HAECs (not treated with the nanoparticles of Au-Am-PAPS), showing caveolae in cytosol of HAECs. Caveolae in cytosol of HAECs were detected by immunostaining of caveolin-1 using rabbit anti-caveolin-1 IgG and gold nanoparticles (10 nm of diameter) conjugated anti-rabbit IgG. Gold nanoparticles with 10 nm of diameter were specifically accumulated around the outer perimeter of round-shape structures with diameters of about 100 nm (Figure 4c). The result of immunodetection of caveolae indicates that the round shape structures in cytosol of HAECs are caveolae and provides an evidence that nanoparticles of Au-Am-PAPS are trapped in caveolae. Thus, the ultrathin section image of HAECs indicates that the nanoparticles of Au-Am-PAPS are trapped in caveolae at the plasma membrane of HAECs and are internalized into cytosol of HAECs. In addition to the nanoparticles trapped in caveolae, dark spots with a diameter of 5−10 nm (surrounded by circle in Figure 4b) were confirmed in cytosol of HAECs (Figure 4b). These spots are assigned to gold nanoparticles attached to amphiphilic polysiloxane (Au-Am-PAPS). The different localization of polysiloxane nanoparticles in cytosol of HAECs suggests that there are at least two different pathways in the cellular uptake of polysiloxane nanoparticles: caveolae and the other pathways, including clathrin-coated pits and macropinocytosis. Furthermore, we observed the undercoat structure on the cytoplasmic surface of the upper cell membrane using rapid-freeze deep-etch immunoreplication so as to obtain a detailed view of the cellular uptake of the nanoparticles via caveolae as main endocytic pathways for the uptake of polysiloxane nanoparticles. Fine structures of plasma membrane such as filamentous netlike structure of actin filaments, clathrin coated pits, and caveolae can be preserved by rapid freezing at the cooling speed of 10^5 °C/sec in specimen preparation. The extreme cooling speed does not cause any ice nucleation that can damage the organized structure of the membrane skeleton. In a recent study by Morone and Kusumi,[22] they applied the rapid-freeze replication method to the electron microscopy observation of the membrane skeleton and succeeded in viewing the fine structure of the membrane skeleton with nanometer scale resolution and demonstrating that the membrane skeleton mesh corresponds to the membrane compartment model that was suggested by the study of the diffusion of membrane molecules. Figure 4d and e are TEM images of the undercoat structure of the bottom cell membrane of HAECs before and after the exposure to the nanoparticles of Flu-Am-PAPS. The images were taken using a specimen that was processed by the rapid-freeze and deep-etch method. Caveolae (the characteristic striated round structures: 50−100 nm in diameter), clathrin-coated pits (the characteristic basket-like structures: 100−200 nm in diameter), and actin filaments were confirmed in the upper cell membrane of the intact HAECs (Figure 4d). The nanoparticles of Flu-Am-PAPS endocytosed

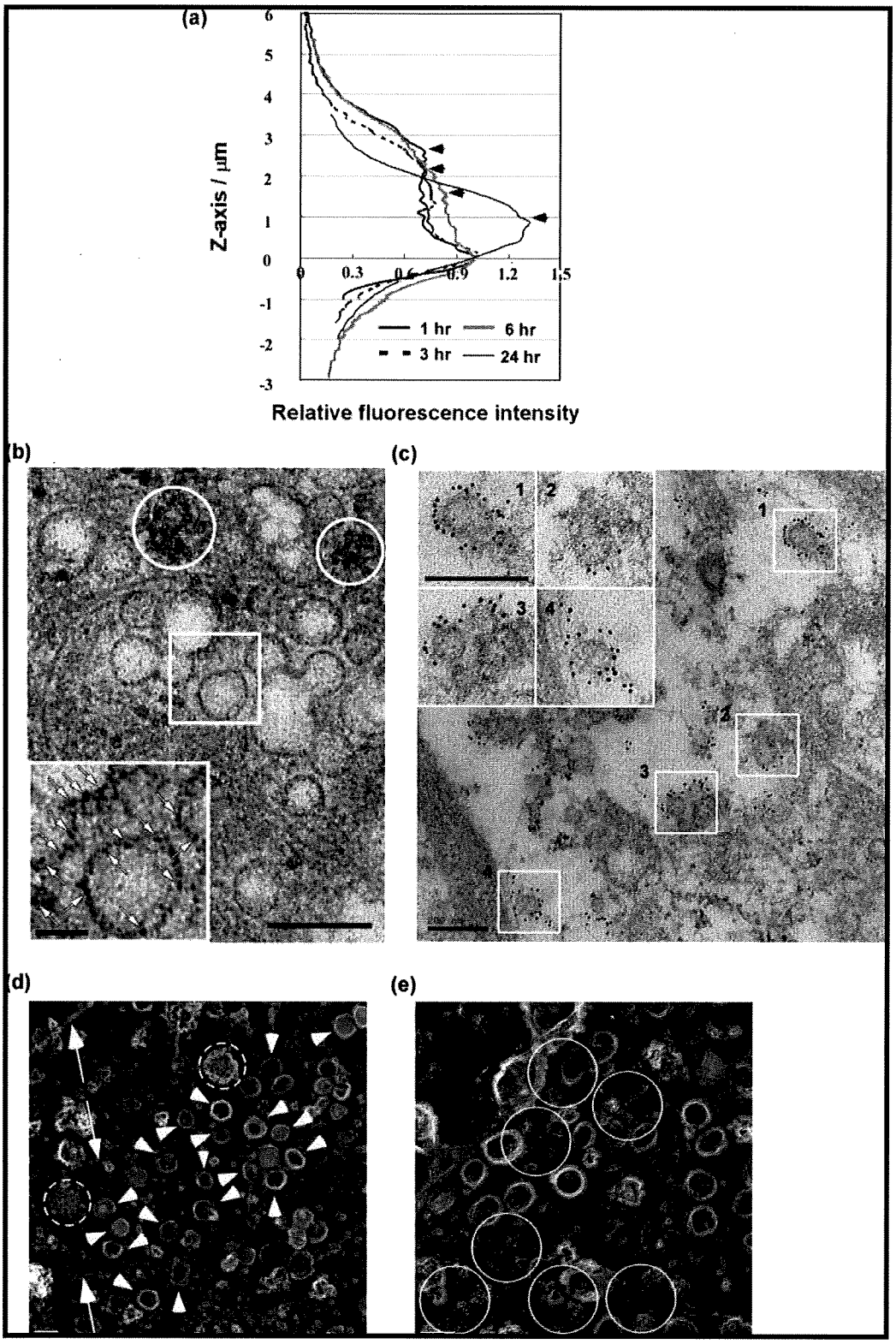

Figure 4. Internalization of nanoparticles of Flu-Am-PAPS in HAECs. (a) F.I. profiles of Flu-Am-PAPS in HAECs. F.I. was calculated by integrating brightness at each pixel over an optical section of confocal fluorescence image. The F.I. is plotted against the *Z*-axis position of each optical section in a confocal fluorescence image. Arrow heads indicates the intensity maximum in the profiles. The intensity maximum can reflect the most probable location of nanoparticles of Flu-Am-PAPS in HAECs at each incubation time. TEM observation of caveolae-mediated endocytosis in HAECs. Ultrathin sections were cut out from embedded HAECs in the direction parallel to the culture dish surface. In the ultrathin section image (b) the nanoparticles of Au-Am-PAPS were incorporated into cytosol of HAECs. Small black dots derived from gold nanoparticles attached to the amphiphilic polysiloxane with diameter of 5−10 nm are confirmed in the inner perimeter of caveolae (indicated by square). The inset is a two-times magnified image of the area indicated by square and shows clearly the small black dots in caveolae (indicated by arrows); (c) immunodetection of caveolae structures in cytosol of HAECs. Caveolae were confirmed by specific accumulation of 10 nm gold nanoparticles of secondary IgG (dark black dots) around the round structures with diameters of 100 nm in cytosol. Scale bars in Figure (b) and (c) represent 200 nm. Scale bars in the insets are 100 nm in (a) and 200 nm in (b). Rapid-freeze, deep-etch immunoreplication TEM images ((d) and (e)) show the undercoat structure of the upper cell membrane enriched in caveolae (indicated by arrow heads), (d), and the gold nanoparticles (white spots in circles) indicating the existence of the Flu-Am-PAPS in the caveolae-enriched area, (e). Other fine structures in (d) are clathrin coated pits (indicated by circle with broken line) and filamentous actin (indicated by arrow). Scale bar: 100 nm.

by HAECs were detected by indirect immunolabeling method with 5 nm diameter colloidal gold particles. Figure 4e shows that the gold particles for immunolabeling of Flu-Am-PAPS that were identified as the dispersed white spots in the TEM image appeared on the internal face of the upper cell membrane and that the gold particles were localized in the area where caveolae were densely accumulated (Figure 4e). The localization of gold particles in cell membrane means that the nanoparticles of Flu-Am-PAPS are localized in the caveolae accumulated area of the upper cell membrane and strongly suggests that caveolae can function as pathways in endocytosis when the nanoparticles of Flu-Am-PAPS are endocytosed into HAECs.

As for the particle size of the endocytosed nanoparticles, we extracted the endocytosed nanoparticles (Flu-Am-PAPS) from HAECs by using a surfactant free protein extraction method and measured the size of the extracted nanoparticles by DLS. According to the histogram of the particle size of the extracted nanoparticles in cytoplasmic fraction of HAECs (the histogram data are attached to Supporting Information as Figure S2), the histogram peak corresponding to the intact nanoparticles of Flu-Am-PAPS (the histogram peak at 150 nm in Figure S2b) shifted to smaller particle size (the histogram peak at 100 nm in Figure S2a) after the endocytosis into HAECs. This suggests that the nanoparticles of Flu-Am-PAPS comparable to the caveolae size are preferentially endocytosed by HAECs. Furthermore, we performed a DLS measurement of the collected sample including serum proteins of growth medium, nanoparticles of Flu-Am-PAPS, and cell debris after the incubation with HAECs and found that the histogram peak of the polysiloxane nanoparticles shifted from 150 nm (before incubation) to 250 nm (the histogram peak in Figure S2c) after the incubation with HAECs. This suggests that the polysiloxane nanoparticles that are larger than the caveolae size are more difficult to be endocytosed and remain after the incubation with HAECs. From the above experiment data of immunofluorescence microscopy, electron microscopy, and particle size measurement, it can be concluded that nanoparticles of amphiphilic polysiloxanes comparable to caveolae size are endocytosed via caveolae in plasma membrane of HAECs.

NO Release in HAECs. NO is a vasodilator synthesized in endothelial cells and plays important physiological roles such as the regulation of blood pressure and the inhibition of platelet adhesion.[7] As we mentioned the endocytic pathways for the uptake of the nanoparticles, caveolae are main routes in endocytosis and gateways to signal-transducing domain where inactive eNOS molecules are localized. It is an intriguing question whether the uptake of the nanoparticles can work in the activation of eNOS, if so, how it does. To study the influence of the nanoparticles on the expression of cell function, nitric oxide release of HAECs was monitored by using diaminorhodamine-4 acetoxymethyl ester (DAR-4 M AM), a fluorescent indicator for NO.[18] DAR-4 M AM can permeate through plasma membrane, be distributed to cytosol, specifically react with NO, and form a fluorescent triazole compound. HAECs were exposed to Dulbecco's modified Eagle medium containing 50 μM DAR-4 M AM for 10 min after the 6 h incubation with nanoparticles of Am-PAPS (0.1 mg/mL). NO release followed by the cellular uptake of polysiloxane nanoparticles could be detected by fluorescence microscope observation of the fluorescence intensity change that results from the triazole compound formation. Figure 5 shows the time profiles of fluorescence intensity of the reaction product derived from NO release after the incubation with nanoparticles (closed triangle), the treatment with bradykinin, endogenous eNOS activator (open circle), the incubation

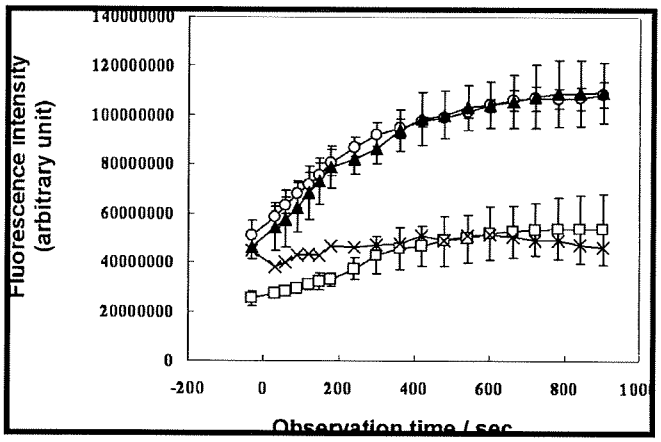

Figure 5. NO release in HAECs. Time profiles of NO release of HAECs. NO was detected by fluorescent indicator, diaminorhodamine-4 acetoxymethyl ester (DAR-4 M AM). The profile represented by open circles shows the NO release after the stimulation with bradykinin ($n = 4$). The profile represented by closed triangles shows the NO release after the cellular uptake of the nanoparticles of amphiphilic polysiloxane ($n = 4$). The profile represented by open squares shows the NO release after the cellular uptake of the sugar conjugated water-soluble polysiloxane ($n = 3$). The NO release profile in resting HAECs was indicated by cross ($n = 3$). The error bar in each data point is represented by standard deviation.

with water-soluble polysiloxane for positive control (open square), and the incubation in DMEM for negative control (cross symbol). After the uptake of nanoparticles, NO release of HAECs was enhanced up to the same release level that was observed when endothelial cells were stimulated by bradykinin. As a preliminary study about the effect of other nanomaterials on NO release in HAECs, we tested NO release level using commercially available polystyrene nanoparticles, micromer (Micromod, Rostock, Germany) in comparison with that using our polysiloxane nanoparticles. A similar trend in NO release was observed when HAECs were incubated with a growth medium containing 1 mg/mL of the polystyrene nanoparticles with 50 nm of diameter (time profile of NO release represented by open squares of Figure S3 in Supporting Information). However, the polystyrene nanoparticles with 200 nm of diameter did not enhance NO release level (time profile of NO release represented by closed squares of Figure S3 in Supporting Information). This suggests that nanoparticles with caveolae size could enhance NO release in HAECs. Furthermore, NO release followed by 6 h incubation with a nonassociative water-soluble sugar conjugated polysiloxane (Figure 1b; concentration, 1 mg/mL) was less than half of the NO release level induced by the amphiphilic polysiloxane nanoparticles and exhibited a time profile that was quite similar to that without stimulation (negative control: cross symbols in Figure 5). As a result of these data, the enhanced release of NO after the incubation with polysiloxane nanoparticles suggests that signal transduction leading to NO release is activated upon the cellular uptake of the nanoparticles via caveolae.

Activation of Endothelial Nitric Oxide Synthase (eNOS) Coupled to Nanoparticle Uptake. In resting endothelial cells, some of the eNOS molecules are inhibited by protein complex formation with caveolin-1, a constituent protein of caveolae. Cell stimulation with Ca^{2+}-mobilizing agonists such as bradykinin promotes calmodulin binding to eNOS and dissociation of eNOS from caveolin-1. The dissociated eNOS molecules can be detected in intracellular sites close to nucleus.[23] Such a subcellular migration of signaling proteins followed by their activation is known as translocation. The translocation of eNOS

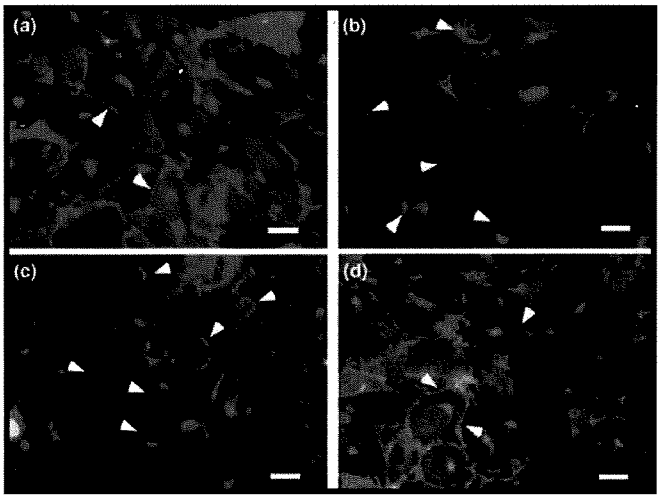

Figure 6. Translocation of eNOS in HAECs in response to bradykinin and upon cellular uptake of the nanoparticles of Am-PAPS. (a) Representative image of eNOS localization in resting HAECs (arrowhead). eNOS was redistributed from the cell periphery to intracellular sites near the nucleus (arrowheads in (b) and (c)) when HAECs were treated with 1 μM bradykinin for 5 min, (b), or were incubated with the nanoparticles of Am-PAPS (0.1 mg/mL) for 6 h, (c). eNOS did not translocate to peri-nuclear region of HAECs when HAECs were exposed to sugar conjugated water-soluble polysiloxane (1 mg/mL) for 6 h, (d). Scale bar in each image is 20 μm.

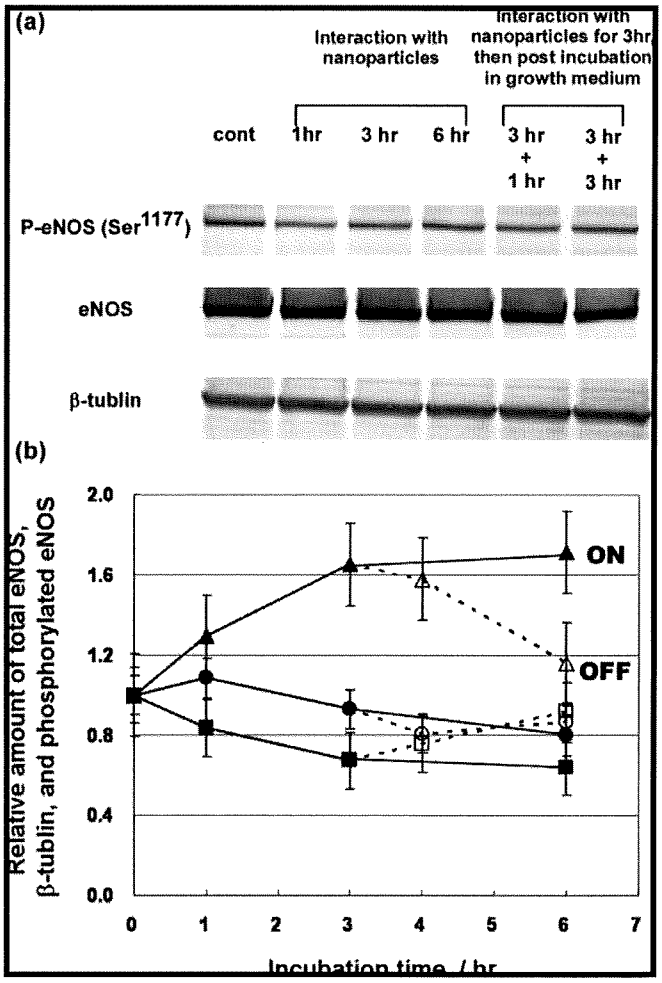

Figure 7. Nanoparticles of amphiphilic polysiloxane (Am-PAPS) stimulate phosphorylation of eNOS. HAECs were incubated with nanoparticles of Am-PAPS for the time period indicated. (a) Cell lysates were analyzed by Western blot with antibodies for phosphorylated eNOS-Ser1177, eNOS, and β-tubulin. (b) The bands of target proteins were quantified by measuring the colorimetric intensity. The graph shows the time course of the expression level of the target proteins (▲, △: P-eNOS, ■, □: e-NOS, and ●, ○: β-tubulin). The time courses represented by closed symbols demonstrate the expression level of the proteins of interest during the incubation with polysiloxane nanoparticles. The time course of the proteins of interest after the removal of polysiloxane nanoparticles at 3 h of incubation are depicted by open symbols and dotted lines. Each data point represents the means ± SE (n = 3).

is followed by the activation of eNOS in endothelial cells.[23] Phosphorylation of eNOS on Ser^{1177} occurs concomitantly in the activation process of eNOS.[24] Here we studied the influence of nanoparticle uptake of HAECs on the eNOS activation with respect to the intracellular translocation and the phosphorylation of eNOS. Immunofluorescence imaging of HAECs using monoclonal antibody to eNOS demonstrated that eNOS bound to cell membrane (cell periphery: Figure 6a) translocate to the cell cytosol and the peri-nuclear region upon 5 min stimulation with 1 μM of bradykinin (Figure 6b). The translocation of eNOS was confirmed as ring-like patterns around nucleuses after the HAECs were exposed to nanoparticles of Am-PAPS for 6 h (Figure 6c). This suggests that caveolae-mediated endocytosis of nanoparticles in HAECs can be coupled to the eNOS activation and can work as an external stimuli in a signal transduction where membrane-bound eNOS are activated. Phosphorylation of eNOS at Ser^{1177} (P-eNOS) was detected by Western blot analysis. Figure 7a shows that phosphorylation of eNOS occurred when HAECs were incubated with the nanoparticles of Am-PAPS. The target proteins (eNOS and P-eNOS) transferred to PVDF membranes were detected by colorimetric reaction of TMB substrate. The protein levels of the target proteins were evaluated by measuring the intensity of the reaction product stained on the blotted bands. In Figure 7b the target protein levels were plotted against time of the incubation with nanoparticles. The total amount of eNOS gradually decreased to 65% of the initial amount of eNOS at 6 h of incubation while HAECs were incubated with polysiloxane nanoparticles (the time profile of eNOS: closed squares in Figure 7b). β-Tubulin, a loading control for Western blot analysis, exhibited a slight decrease in expression level during the incubation with polysiloxane nanoparticles (the time profile of β-tubulin: closed circles in Figure 7b), although the same amount of extracted proteins (2 μg) was applied to each lane in SDS-PAGE. This indicates that incubation with polysiloxane nanoparticles influences the expression level of eNOS in HAECs. On the other hand, the P-eNOS (Ser^{1177}) level gradually increased by 1.3 fold at 1 h of incubation and by 1.6-fold at 3 h from the initial phosphorylation level of eNOS (the time profile of P-eNOS: closed triangles in Figure 7b). The expression level of P-eNOS reached saturation point at 6 h of incubation with polysiloxane nanoparticles. Thus, the activation of eNOS was followed by the cellular uptake of polysiloxane nanoparticles and the expression level of P-eNOS was maintained as long as HAECs were exposed to the nanoparticles. Furthermore, the expression levels of target proteins (eNOS, P-eNOS, and β-tubulin) were back to the initial level of each protein (time profiles (from 3 to 6 h of incubation time) indicated by open symbols and dotted lines in Figure 7b) when polysiloxane nanoparticles were removed from culture medium and HAECs were incubated in a fresh growth medium for 3 h after the removal of nanoparticles. These data suggest that phosphorylation of eNOS at Ser^{1177} is stimulated by interaction with nanoparticles and the enhanced level of phosphorylation is maintained transiently during the interaction with polysiloxane nanoparticles. Meanwhile, any eNOS translocation was not

observed at all when HAECs were exposed to the water-soluble sugar conjugated polysiloxane (concentration: 1 mg/mL) for 24 h (Figure 6d). According to the result of fluorescence image analysis for the estimation of the amount of the endocytosed polymers, the amount of the incorporated water-soluble polysiloxane at 24 h of the incubation was approximately 15% of that of the incorporated fluorescein-labeled nanoparticles (Flu-Am-PAPS) at 6 h of the incubation time (Figure S4 is available at Supporting Information). The water-soluble polysiloxane was certainly endocytosed by HAECs; however, the eNOS activation did not occur. These results suggest that the types of the polymers (nonassociative polymer chains or nanoparticles of amphiphilic polymers) exposed to cells and the pathways (caveolae or clathrin coated pits) selected in endocytosis are important factors that can influence the signal transduction in the regulation of cell function. Thus, we assume that the delivery of the nanoparticles targeted to caveolae facilitates eNOS activation (subcellular translocation and phosphorylation at Ser^{1177}) and the activated eNOS promotes NO release. The details of the mechanism underlying the eNOS activation upon the caveolae-mediated endocytosis of our polysiloxane nanoparticles is still under investigation and will be reported elsewhere.

Conclusion

In conclusion, the nanoparticles of amphiphilic polysiloxane were endocytosed via caveolae in human aortic endothelial cells and the uptake of the nanoparticles promoted nitric oxide release in HAECs. Caveolae is a membrane microdomain where various signal transduction molecules are accumulated and external stimuli are processed. Endothelial nitric oxide synthase is one of the constituent molecules in signal transduction and plays a significant role in regulation of vasorelaxation by synthesizing nitric oxide. Some of eNOS molecules are bound to caveolin-1 and deactivated in caveolae. Activation of eNOS is triggered in vivo by binding of physiological active molecules such as bradykinin, angiotensin-II, and estrogen to their corresponding receptors in endothelial cells. According to the recent study by Maniatis et al., eNOS-dependent NO production is coupled to caveolae-mediated endocytosis induced by albumin binding protein gp60 (albumin receptor).[25] In their case, NO release started just after gp60 activation by adding BSA and lasted up to 20 min. Phosphorylation of eNOS accompanied by gp60 activation was confirmed at just 30 s after the addition of BSA. This means that BSA uptake via caveolae in rat lung microvascular endothelial cells is quickly processed as an external signal and leads to NO release. In our study, a delay of 15−60 min between the beginning of the nanoparticle uptake and the onset of the induced phosphorylation of eNOS was observed. This kind of delay was rather observed in the phosphorylation of eNOS that was stimulated by shear stress to bovine aortic endothelial cells.[26] Sustained phosphorylation of eNOS is another feature of eNOS activation that is followed by nanoparticle uptake of HAECs. We found that the phosphorylation of eNOS lasted while HAECs were exposed to nanoparticles for 6 h. The phosphorylation of eNOS induced by gp60 activation lasted at most for 30 min. Furthermore, there was considerable difference in the working concentration of stimulants for the activation of eNOS between BSA (5 mg/mL) and our nanoparticles (0.1 mg/mL or less). We think that there are some different mechanisms in the activation of eNOS induced by caveolae-mediated endocytosis between former study using BSA and our current study using artificial nanoparticles. In any case, nanoparticle uptake by HAECs stimulates the activation of eNOS and raises the NO production. This means that nanoparticles can be regarded as extracellular signals. Concerning the influence of the interaction between nanomaterials with cells on the expression of cell function, a study on the behavior of bovine carotid arterial endothelial cells cultured on polyurethane nanocomposites demonstrated that cell migration could be regulated by the surface morphological change induced by blending gold nanoparticles with polyurethane and revealed that the promoted migration was associated with up-regulation of eNOS expression via the activation of PI3K/Akt signaling pathway.[27] The key phenomena explaining the promoted cell migration is signal transduction associated with the interaction between cells and the nanostructured surface and concomitant rearrangement of cytoskeleton. Meanwhile, our study deals with signal transduction associated with endocytosis of nanoparticles that are targeted to membrane microdomains of cells. As far as we know, this is the first demonstration that nitric oxide release in HAECs can be induced by the caveolae-mediated cellular uptake of artificial nano materials of synthetic polymer and that the uptake itself can work as external stimuli leading to the expression of a cell function. Thus, nanoparticle can work as an artificial signal substance whose signaling characteristics may be tuned by molecular design of constituting amphiphilic polymers as well as the nanoparticles can be used as nanocarriers in drug delivery system. In the drug delivery system the nanocarrier itself should be inert to targeted cells and tissues. However, as we demonstrated in this study, nanoparticles can influence cell functions; nanoparticles may not only promote the pharmacological effects of delivered drugs but also cause undesirable effects in the target tissues or cells. The molecular design of constituent molecules for nanoparticles and the interaction between nanoparticles and cells should be considered more carefully in terms of the activation of cell functions. Nevertheless, we expect that targeting delivery of nanoparticles including our polysiloxane nanoparticles to caveolae is a potential and novel medication to hypertension based on the regulation of NO release by switching of eNOS activation in a single cell.

Acknowledgment. T.N. thanks Professor Mitsuru Akashi and Dr. Takami Akagi of Osaka University for allocating instrument time of dynamic light scattering measurement, Dr. Tetsuji Yamaoka and Dr. Atsushi Mahara of National Cardiovascular Center Research Institute for allocating instrument time of fluorescence spectroscopy measurement, Dr. Tsutomu Furuzono of National Cardiovascular Center Research Institute for allocating instrument time of microplate reader in protein assay, and Mrs. Mina Kaneko for technical work in cell culture experiments. Part of this research was financially supported by Terumo Life Science Foundation in fiscal year of 2008.

Supporting Information Available. Supplementary data of nanoparticle size change in physiological condition, size of nanoparticles endocytosed, and cellular uptake of water-soluble polysiloxane. This material is available free of charge via the Internet at http://pubs.acs.org.

References and Notes

(1) Simons, K.; Ikonen, E. *Nature* **1997**, *387*, 569–572.
(2) Minshall, R. D.; Sessa, W. C.; Stan, R. V.; Anderson, R. G. W.; Malik, A. B. *Am. J. Physiol.* **2003**, *285*, L1179–L1183.
(3) Gratton, J.-P.; Bernatchez, P.; Sessa, W. C. *Circ. Res.* **2004**, *94*, 1408–1417.
(4) Wyatt, A. W.; Steinert, J. R.; Mann, G. E. *Biochem. Soc. Symp.* **2004**, *71*, 143–156.

(5) Vallance, P.; Chan, N. *Heart* **2001**, *85*, 342–350.
(6) McIntosh, D. P.; Tan, X.-Y.; Oh, P.; Schnitzer, J. E. *Proc. Natl. Acad. Sci. U.S.A.* **2002**, *99*, 1996–2001.
(7) Michel, T. *Braz. J. Med. Biol. Res.* **1999**, *32*, 1361–1366.
(8) Muro, S.; Koval, M.; Muzykantov, V. *Curr. Vasc. Pharmacol.* **2004**, *2*, 281–299.
(9) Sanvicens, N.; Marco, M. P. *Trends Biotechnol.* **2008**, *26*, 425–433.
(10) Conner, S.; Scmid, S. L. *Nature* **2003**, *422*, 37–44.
(11) Cruz, T.; Gaspar, R.; Donato, A.; Lopes, C. *Pharm. Res.* **1997**, *14*, 73–79.
(12) Mark, J. E.; Allcock, H. R.; West, R. In *Inorganic Polymers*, 2nd ed.; Oxford University Press: New York, 2005; pp 154−199.
(13) Kichler, A.; Sabourault, N.; Décor, R.; Leborgne, C.; Schmutz, M.; Valleix, A.; Danos, O.; Wagner, A.; Mioskowski, C. *J. Controlled Release* **2003**, *93*, 403–414.
(14) Moghimi, S. M.; Hunter, A. C.; Murray, J. C. *Pharmacol. Rev.* **2001**, *53*, 283–318.
(15) Beppu, K.; Kaneko, Y.; Kadokawa, J.; Mori, H.; Nishikawa, T. *Polym. J.* **2007**, *39*, 1065–1070.
(16) Tominaga, H.; Ishiyama, M.; Ohseto, F.; Sasamoto, K.; Hamamoto, T.; Suzuki, K.; Watanabe, M. *Anal. Commun.* **1999**, *36*, 47–50.
(17) Heuser, J. *Traffic* **2000**, *1*, 545–552.
(18) Kojima, H.; Hirotani, M.; Nakatsubo, N.; Kikuchi, K.; Urano, Y.; Higuchi, T.; Hirata, Y.; Nagano, T. *Anal. Chem.* **2001**, *73*, 1967–1973.
(19) Kaneko, Y.; Iyi, N.; Kurashima, K.; Matsumoto, T.; Fujita, T.; Kitamura, K. *Chem. Mater.* **2004**, *16*, 3417–3423.
(20) Durin, G.; Cottin, S.; Blanc, E.; Rees, A. R.; Temsamani, J. *J. Biol. Chem.* **2003**, *278*, 31192–31201.
(21) Drab, M.; Verkade, P.; Elger, M.; Kasper, M.; Lohn, M.; Lauterbach, B.; Menne, J.; Lindschau, C.; Mende, F.; Luft, F. C.; Schedl, A.; Haller, H.; Kurzchalia, T. V. *Science* **2001**, *293*, 2449–2452.
(22) Morone, N.; Fujiwara, T.; Murase, K.; Kasai, R.; Ike, H.; Yuasa, S.; Usukura, J.; Kusumi, A. *J. Cell Biol.* **2006**, *174*, 851–862.
(23) Prabhakar, P.; Thatte, H. S.; Goetz, R. M.; Cho, M. R.; Golan, D. E.; Michel, T. *J. Biol. Chem.* **1998**, *273*, 27383–27388.
(24) Fleming, I.; Busse, R. *Am. J. Physiol.* **2003**, *284*, R1–R12.
(25) Maniatis, N.; Brovkovych, V.; Allen, S. E.; John, T. A.; Shajahan, A. N.; Tiruppathi, C.; Vogel, S. M.; Skidgel, R. A.; Malik, A. B.; Minshall, R. D. *Circ. Res.* **2006**, *99*, 870–877.
(26) Boo, Y. C.; Sorescu, G.; Boyd, N.; Shiojima, I.; Walsh, K.; Du, J.; Jo, H. *J. Biol. Chem.* **2002**, *277*, 3388–3396.
(27) Hung, H. S.; Wu, C. C.; Chien, S.; Hsu, S. H. *Biomaterials* **2009**, *30*, 1502–1511.

BM900128X

Experimental Neurology 221 (2010) 175–185

Contents lists available at ScienceDirect

Experimental Neurology

journal homepage: www.elsevier.com/locate/yexnr

Chronic stress-mutated presenilin 1 gene interaction perturbs neurogenesis and accelerates neurodegeneration

Shohko Kunimoto [a,*], Shun Nakamura [a,1], Keiji Wada [b], Takayoshi Inoue [a]

[a] Department of Biochemistry and Cellular Biology, National Institute of Neuroscience, National Center of Neurology and Psychiatry, Tokyo 187-8502, Japan
[b] Department of Degenerative Neurological Diseases, National Institute of Neuroscience, National Center of Neurology and Psychiatry, Tokyo 187-8502, Japan

ARTICLE INFO

Article history:
Received 30 July 2009
Revised 23 October 2009
Accepted 28 October 2009
Available online 4 November 2009

Keywords:
Neurodegenerative disease
Gene–environment interaction
Chronic intermittent restraint stress (CIRS)
Doublecortin (DCX)
Presenilin 1 (PS1)
Neurogenesis

ABSTRACT

Recent evidence suggests that supplemental factors coincident with aging and genetic determinants might be involved in the initial progression of Alzheimer's disease (AD). Early studies also indicate that chronic stress decreases hippocampal neurogenesis. Here, we investigate the effect of chronic stress on hippocampal neurogenesis using a transgenic mouse line (Tg) that overexpresses human presenilin 1 (PS1) with a familial AD (FAD)-related mutation in order to elucidate how the combination of chronic stress and mutated genes affects the cytoarchitecture in the hippocampal granule cell layer (GCL), which contributes to spatial learning and memory. Using an original chronic intermittent restraint stress (CIRS) protocol, we examined the effect of stress on hippocampal neurogenesis and neurodegeneration by immunohistochemical analysis. After short-term CIRS, neurodegeneration in Tg mice was significantly increased in the hippocampus with an earlier onset and progression than in the non-stressed Tg mice. Moreover, after long-term CIRS, transitional neurodegeneration appeared to proceed along the neuronal circuit involved in cognitive function in stressed Tg mice. Although the number of Pax6-positive (+) cells (mostly granule neuron precursors) did not significantly decrease during CIRS in both non-Tg and Tg mice, doublecortin (DCX) + neuronal progenitor cells in the GCL were markedly influenced in Tg mice; they were significantly reduced without stress compared with non-stressed non-Tg mice and significantly increased by CIRS compared with non-stressed Tg mice. We conclude from these results that diverse responses against stressful experiences among genetically predisposed individuals could lead to cognitive dysfunction through retardation of neuronal maturation and neurodegeneration.

Introduction

In human aging processes, frontal–striatal structural changes of the brain have been suggested to underlie mild memory difficulties. In Alzheimer's disease (AD) patients, cellular pathology characterized by amyloid plaques/neurofibrillary tangles (Golde et al., 2000; Mattson, 2004) results in progressive neurodegeneration and atrophy within medial temporal brain structures that associate with cognitive functions (Jack et al., 1992; Killiany et al., 1993); this leads directly to memory impairment via separate mechanisms (Buckner, 2004). At the molecular level, genetic mutations of presenilin 1 and 2 (PS1, PS2) or missense mutations in amyloid precursor protein increase amyloid β deposition, which are well investigated pathogenic traits of AD (Masters and Beyreuther, 1998). In addition, recent studies have highlighted the significance of adult neurogenesis in the hippocampal granule cell layer (GCL) for cognitive memory (Bruel-Jungerman et al., 2005; Drapeau et al., 2003; Gould et al., 1999; Imayoshi et al., 2008; Kempermann and Gage, 2002; Shors et al., 2001; Zhang et al., 2008), and an acceleration of neurogenesis has indeed been expected to provide therapeutic measures against cognitive impairment in AD (Kuhn et al., 2007; Ogita et al., 2005). In light of the progressive neurodegeneration seen in AD patients, even with increased generation of neuronal progenitor cells in the GCL (Jin et al., 2004), the elucidation of additional factors in granule cell regeneration is essential for clinical applications.

Several lines of evidence have thus far implied a correlation between the stress-induced decrease in hippocampal neurogenesis and deficits in the hippocampus-related memory (Gould and Tanapat, 1999; Nagata et al., 2009; Pardon and Rattray, 2008; Sandi, 2004;

Abbreviations: BrdU, 5-bromo-2′-deoxyuridine; AD, Alzheimer's disease; ANOVA, analysis of variance; CIRS, chronic intermittent restraint stress; CA3, Cornus Ammonis 3; DG, dentate gyrus; DCX, doublecortin; FAD, familial Alzheimer's disease; GCL, granule cell layer; NS, non-stressed control mice; PBS, phosphate buffered saline; PCtx, piriform cortex; +, positive; PS1, presenilin 1; RCtx, retrosplenial cortex; SEM, standard error of the mean; ST, stressed mice; SGZ, subgranular zone; L/V-Tg, transgenic mouse model of AD with overexpression of an FAD-type PS1; non-Tg, transgenic-negative mouse; W, week-old.

* Corresponding author. Present address: Department of Vascular Dementia Research, National Institute for Longevity Sciences, National Center for Geriatrics and Gerontology, 36-3 Gengo, Morioka-machi, Obu City, Aichi 474-8522, Japan. Fax: +81 562 46 8438.
E-mail address: kunimoto@nils.go.jp (S. Kunimoto).
[1] Present Address: Department of Biotechnology and Life Science, Tokyo University of Agriculture and Technology, 2-24-16 Naka-chou, Koganei-city, Tokyo 184-8588, Japan.

0014-4886/$ – see front matter © 2009 Elsevier Inc. All rights reserved.
doi:10.1016/j.expneurol.2009.10.020

Veena et al., 2009). Furthermore, chronic stress accelerates cognitive impairments and increases amyloid deposition in APPV717I-CT100 mice overexpressing the familial AD (FAD) V717I "London" mutation within the carboxyl terminus of human amyloid precursor protein (Jeong et al., 2006). However, the combinatorial effect of chronic stress and mutated genes on the hippocampal neurogenesis is not fully understood. Here we hypothesize that, in individuals predisposed to genetic mutations for AD, a mutated gene–environmental stress interaction might synergistically deteriorate the level of hippocampal neurogenesis, leading to precocious cognitive impairment. To test this hypothesis, we selected a transgenic mouse model of AD with overexpression of an FAD-type PS1 (L286V) (L/V-Tg); these mice accumulate abnormal amyloid β in the cytoplasm to bring about massive cell degeneration without formation of amyloid plaques after 6 months of age (Chui et al., 1999). We exposed this genetically predisposed mouse to stressful environments and found that the number of degenerating neurons was increased in the brain regions involved in cognitive function (i.e., the hippocampus) earlier in stressed mice than in non-stressed mice, and neurogenesis was affected differently by stress in the Tg and non-Tg mice. These data suggest that diverse responses to stressful experiences among genetically predisposed individuals might affect neurogenesis and neurodegeneration. We propose that mice that display hallmarks of AD late in life with conditioned environmental factors could be used as an animal model for the analysis of the onset and progression of AD.

Materials and methods

Animals

A transgenic mouse line overexpressing human PS1 with an FAD-related mutation of leucine 286 to valine (L286V) under the control of the human PDGF-β promoter (Chui et al., 1999) had been originally produced by Dr. Chui et al. at the National Institute of Neuroscience (NCNP, Tokyo, Japan). The mouse line was maintained in the FVB/N background and was back-crossed to obtain male hemizygous mice (L/V-Tg) at the NCNP. In the brains of transgenic mice older than 13 months (aged mice), neurodegeneration was significantly accelerated without amyloid plaque formation, whereas most populations of neurons deposit amyloid β42 intracellularly. Mice were housed under controlled conditions (21 °C room temperature, 60% humidity, lights on from 8:00 am to 8:00 pm) with food and water available *ad libitum*. Sixty-two young adult (7-week-old) male mice were used in the whole study. All studies were performed by comparing the L/V-Tg mice with the age-matched, transgenic-negative littermates (non-Tg). The Non-Tg and L/V-Tg mice were randomly assigned to the control (NS) or stressed (ST) group [for short-term experiments, non-Tg(NS) ($n=12$), non-Tg(ST) ($n=12$), L/V-Tg(NS) ($n=13$), L/V-Tg (ST) ($n=13$); for long-term experiments, non-Tg(NS) ($n=3$), non-Tg(ST) ($n=3$), L/V-Tg(NS) ($n=3$), L/V-Tg(ST) ($n=3$)]. Animal care and handling were in accordance with institutional regulations and were approved by the Animal Investigation Committee of the National Institute of Neuroscience, Japan, which in turn conforms to the National Institutes of Health guidelines for the care and use of laboratory animals. The number of animals in this study was the minimum required to obtain statistically significant results. The animals were appropriately treated and anesthetized with Nembutal (Dainippon Sumitomo Pharma Co., Osaka, Japan, 0.25 mg/g of pentobarbitone) to minimize their suffering.

Chronic intermittent restraint stress (CIRS)

Young adult (7-week-old) male mice weighing 25.4±0.5 g for L/V-Tg mice and 24.4±0.5 g for non-Tg mice at the beginning of the stress procedure were used. Mice were housed two to three per cage and were habituated to the experimental room for 10 days without handling. The stressed animals were exposed to restraint stress from 9:30 am to 3:30 pm in their home cage using a well-ventilated restraint tube that fit closely to the mice (Supplementary Fig. 1). For chronic intermittent restraint stress (CIRS), the experimental mice were put into restraint tubes for 6 h every day for 3 weeks (short-term experiments) or 15 weeks (long-term experiments), excluding the weekends (restrained Monday through Friday, rest from 3:30 pm on Friday to 9:30 am on the next Monday). The animals at 11-week-old (short-term) or 23-week-old (long-term) were sacrificed 1 day after the last session (Saturday; Fig. 1). The control mice (NS) were left in their home cage except for handling during weighing and were sacrificed at the same time as the experimental mice (we considered the NS a handled control). Body weight gain was monitored throughout the experiment (three times a week) and, upon termination, the adrenal glands were removed and weighed.

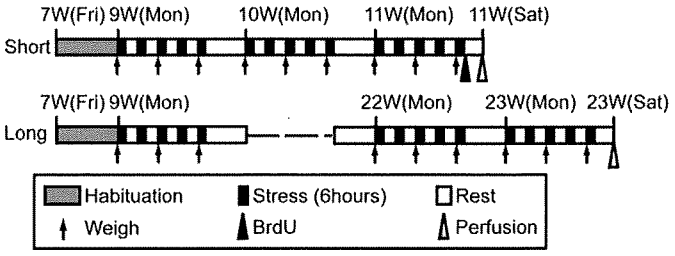

Fig. 1. Protocol summary for short-term (upper) and long-term (lower) chronic intermittent restraint stress (CIRS). For CIRS, each mouse was put into a restraint tube for 6 h every day for 3 weeks (short-term) or 15 weeks (for long-term), excluding weekends, and sacrificed 1 day after the last session (Saturday). For 5-bromo-2′-deoxyuridine (BrdU) labeling, the mice were injected intraperitoneally with BrdU 20 h (for short-term) before perfusion. Fri, Friday; Mon, Monday; Sat, Saturday; W, week-old.

Fixation and histological processing

The animals were perfused transcardially with phosphate buffered saline (PBS, 0.1 M, pH 7.4) followed by 4% paraformaldehyde in PBS. The brains were sagittally cut into halves for post-fixation overnight in the same fixative at 4 °C. The samples were washed in PBS and transferred to an antigen retrieval solution [10 mM sodium citrate, pH 6.0 (Ino, 2003)] for overnight incubation at 4 °C. The samples were then immersed in 300 ml of preheated (95 °C) retrieval solution for 3 min. They were immediately placed in cold 30% sucrose in PBS and incubated at 4 °C overnight. The blocks were immersed in Tissue-Tek OCT Compound (Sakura Fine Technical, Tokyo, Japan), frozen with dry ice, and stored at −80 °C. Cryosections (40 μm thick) cut frontally through the hippocampus using a sliding microtome (Leica CM3000, Leica Microsystems, Bannockburn, IL, USA) were collected sequentially into eight series in a cryoprotectant solution [ethyleneglycol: glycerol:PBS (1:1:2, v/v)] and stored at −20 °C.

Silver staining

For the staining of degenerating neurons, we prepared 8–10 sections from the short-term group [non-Tg(NS) ($n=2$), non-Tg(ST) ($n=2$), L/V-Tg(NS) ($n=2$), L/V-Tg(ST) ($n=2$)] and 12–14 sections from the long-term group [non-Tg(NS) ($n=3$), non-Tg(ST) ($n=3$), L/V-Tg(NS) ($n=3$), L/V-Tg(ST) ($n=3$)]. The mice were perfused as described above. The whole brains were post-fixed for 48 h at 4 °C. Right brain hemispheres were immersed in an embedding medium, frozen with dry ice and stored at −80 °C. Silver staining of cryostat sections was performed using an FD NeuroSilver Kit II (FD NeuroTechnologies, Ellicott City, MD, U.S.A.) according to the manufacturer's protocol to detect degenerating neurons. Sections [Bregma −1.58~−2.92 (Paxinos and Franklin, 2001)] viewed on a video monitor connected to a LEICA DM2500 microscope (×20 NA

0.40 objective) with a LEICA DFC 300-FX digital camera were used for cell counting. The degenerating cells in the dentate gyrus (DG), Cornus Ammonis 3 (CA3), retrosplenial cortex (RCtx), and piriform cortex (PCtx) were counted using the analyze particle mode of Object-Image2.15 (US National Institutes of Health and at the University of Amsterdam). The analytical process was as follows: microscopic color images (each 0.16 mm^2) were opened using the Object-Image2.15 software and through a red channel image, degenerating neurons were selected by density slice mode. The degenerating neurons were always indicated by dense silver precipitates, which appear as black grains in their somata and cells with numerous fine grains in their somata and were counted using the analyze particles mode with several optional settings (i.e. 'minimal particle size of 20 pixels,' 'label particles,' 'outline particles,' 'ignore particles touching edge,' and 'include interior holes'). The numerical density of the degenerating cells was converted to a percentage of the cell number in non-Tg(NS) mice.

Immunohistochemical analysis

Serial sections (40 μm thick) were processed for immunostaining using a primary antibody against Pax6 (Inoue et al., 2000) (anti-Pax6 rabbit antibody 63, 1:500) [non-Tg(NS) ($n=5$), non-Tg(ST) ($n=5$), L/V-Tg(NS) ($n=5$), L/V-Tg(ST) ($n=5$)], Ki-67 (anti-Ki-67 rabbit serum, 1:50;YLEM, Roma, Italy, #PRO229) [non-Tg(NS) ($n=7$), non-Tg(ST) ($n=6$), L/V-Tg(NS) ($n=7$), L/V-Tg(ST) ($n=6$)], or double-cortin (DCX) (anti-DCX guinea pig antibody, 1:3000; Chemicon, CA, USA, #AB5910) [non-Tg(NS) ($n=9$), non-Tg(ST) ($n=8$), L/V-Tg(NS) ($n=9$), L/V-Tg(ST) ($n=8$)]. Free-floating sections were treated first with PBS containing 10% methanol and 3% H_2O_2 for 30 min at room temperature and rinsed in PBS. The sections were next treated with 3% normal goat serum in PBS containing 0.1% Triton X-100 for 2 h at room temperature and incubated for 48 h in the primary antibody solution at 4 °C. Then they were incubated with biotinylated goat anti-rabbit IgG (1:5000; Vector, CA, USA, #BA-1000) for Pax6 and Ki-67 or biotinylated goat anti-guinea pig IgG (1:500; Vector #BA-7000) for DCX for 2 h at room temperature. The immunoreactions with the ABC reagent (Vector) and the ImmunoPure Methal Enhanced DAB Substrate Kit (PIERCE, Rockford, IL, USA) were done according to the manufacturer's protocol. The sections were placed onto an MAS-coated slide glass (Matsunami, Osaka, Japan, #S9443), air-dried, dehydrated with ethanol and xylene, and coverslipped with HSR solution (International Reagents Corp., Kobe, Japan).

BrdU labeling

For the labeling of mitotic cells, the mice received an intraperitoneal injection of 5-bromo-2′-deoxyuridine (BrdU, Sigma, 15 mg/ml dissolved in 0.9% NaCl, 20 μl/g body weight) at 4:30–5:00 pm and were perfused 20 h after injection [non-Tg(NS) ($n=5$), non-Tg(ST) ($n=4$), L/V-Tg(NS) ($n=5$), L/V-Tg(ST) ($n=5$)]. This high dose of BrdU (300 mg/kg) is a specific, quantitative, and nontoxic marker of dividing cells in the adult DG (Cameron and McKay, 2001). Free-floating sections (40 μm thick) were made and incubated in 2 N HCl for 30 min at 37 °C. After being rinsed in borate buffer and PBS, sections were incubated with an anti-BrdU rat monoclonal antibody (1:500, abcam, Cambridge, MA, USA, #ab6326) overnight at 4 °C and then with the secondary antibody for 2 h at room temperature. The immunoreactions with the ABC reagent and DAB were performed as described above.

Quantification and stereology

Serial sections [six sections from each animal, Bregma −1.34 to −3.08 (Paxinos and Franklin, 2001)] (Supplementary Fig. 2) of one hemisphere were taken for stereological quantification of the dentate GCL, including the Pax6-, Ki-67-, DCX-, and BrdU-positive cells in the GCL and subgranular zone (SGZ, a two-cell-thick layer in the granule cell layer, is located close to the hilus or in the lower part of the GCL). For Pax6 or Ki-67 immunostaining, toluidine blue-stained serial sections were used to determine the total volume of the GCL. DAB-stained individual sections were viewed on a video monitor connected to a Zeiss Axiophot 2 microscope (2.5× NA 0.12 objective) with a 3CCD Fuji (Fujifilm, Tokyo, Japan) digital camera. Part of the GCL was delineated by drawing a line, using the programmed tool in Adobe Photoshop7.0 (Adobe Systems Inc., San Jose, CA, USA). The total area of the GCL was measured using Object-Image2.15, and the resultant volume (pixels) was converted into micrometers. Individual cells were visualized using the same system described above (10× NA 0.45 objective), and the marker-positive cells were counted in the GCL, SGZ, and hilus. The cells were counted by an observer blinded to the genotype and the treatment status.

Statistical analyses

For every parameter, the values were first calculated separately for each animal before the means and the standard error of the mean (SEM) were determined for the groups. The number of marker-positive cells in a fixed area (cells/mm^2) was converted to the percentage of the number of marker-positive cells in the non-Tg(NS) littermates. Data are expressed as the mean values ± SEM. All statistical analyses were performed with PRISM version 5.0a (Graph-Pad Software, La Jolla, CA, USA). The data were analyzed by a two-way analysis of variance (ANOVA) between genotypes (non-Tg, L/V-Tg) and treatments (non-stressed, stressed) and with a Bonferroni post hoc test. When an interaction was found, multiple comparisons were performed with the Tukey–Kramer test. Values of $P<0.05$ were considered significant.

Results

Establishment of a chronic intermittent restraint stress model

We first sought to establish an effective restraint tube-based chronic stress model (Supplementary Fig. 1) that causes long-lasting structural changes in the hippocampus. By the protocol with several weeks' continuous restraint stress, it has been pointed out that mice tend to be habituated to the stressor, making it difficult to precisely examine the effects of chronic stress (Kim and Han, 2006). A previous report also indicated that chronic intermittent restraint stress (CIRS) for 2 weeks affected adult neurogenesis in the hippocampus (Rosenbrock et al., 2005). We therefore determined that CIRS is an effective protocol to verify changes in neurogenesis and introduced a resting period during the chronic restraint protocol in which we assess the effectiveness of the stressor using the reduction in body weight gain and the hypertrophy of the adrenal glands as indices.

As a result, our CIRS protocol (Fig. 1) primarily reduced the body growth rate of both non-Tg and L/V-Tg mice under chronic stress (Fig. 2A, B). When the body weight gain, which is expressed as the difference between the end and the beginning of the experiment, was subjected to a two-way ANOVA, we found out a significant effect of treatment ($F_{1,46}=393.98$, $P<0.0001$), but not a genotype effect ($F_{1,46}=1.70$, $P=0.1990$) and no interaction ($F_{1,46}=2.14$, $P=0.1507$) in the short-term experiments. The analysis also revealed a significant effect of treatment ($F_{1,8}=25.66$, $P=0.0010$), but not a genotype effect ($F_{1,8}=0.08$, $P=0.7857$) and no interaction ($F_{1,8}=0.10$, $P=0.7618$) in the long-term experiments. Additionally, the unpaired t-test [non-Tg(ST) vs. L/V-Tg(ST)] revealed that the body weight gain of the L/V-Tg mice (−11.3 ± 0.6%) was significantly reduced compared with that of the non-Tg(ST) animals (−8.6 ± 1.0%) after short-term CIRS (two-tailed, $P=0.0266$; Supplementary Table 1). Although the body growth rate at the resting period was increased in

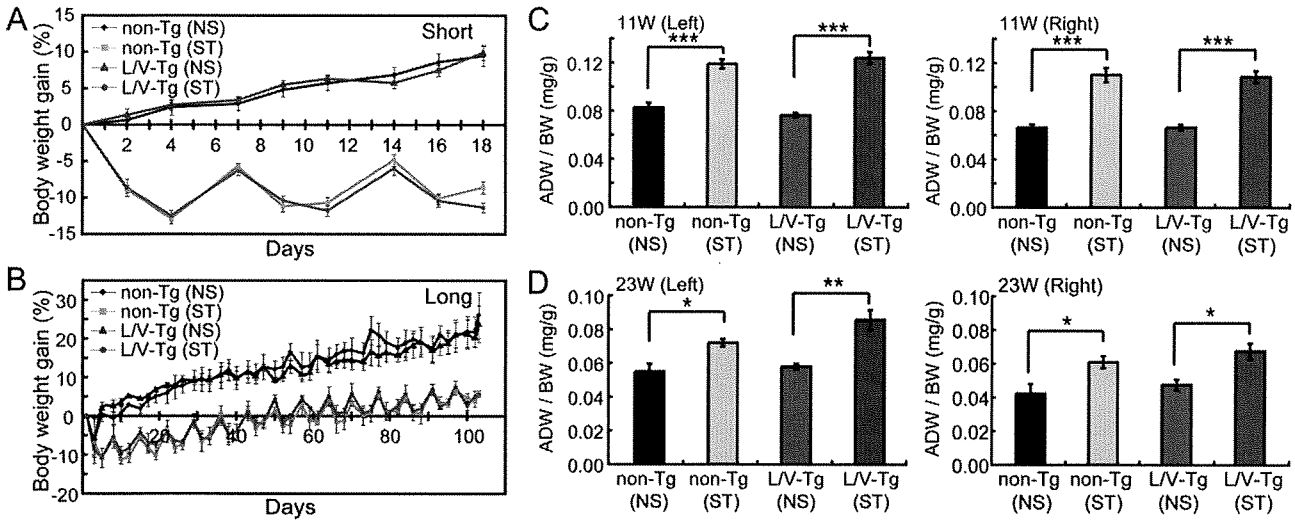

Fig. 2. Chronic intermittent restraint stress (CIRS) induces typical stress symptoms. (A, B) Changes in the body weight gain of mice in the stressed (ST) or non-stressed (NS) groups are plotted; (A) short term; (B) long term. The body weight gain 1 day before perfusion [expressed as the difference between the end and the beginning of the experiment, mean ± standard error of the mean (SEM)] is significantly reduced in stressed animals. (C, D) The left and right adrenal weights after short-term (C) or long-term (D) CIRS are significantly increased in the stressed groups. Data are expressed as the adrenal weight (mg) divided by the body weight (g) (ADW/BW, mean ± SEM). *$P<0.05$, **$P<0.01$, ***$P<0.001$ (Bonferroni, NS vs. ST). Non-Tg, transgenic negative mouse; L/V-Tg, transgenic mouse model of AD with overexpression of an FAD-type PS1; 11W, 11-week-old mice; 23W, 23-week-old mice.

every mouse, the rate of body weight change in the stressed groups showed a distinct fluctuating pattern for 15 weeks compared with that in the non-stressed groups (Fig. 2B). The weight of the right or left adrenal gland was also subjected to a two-way ANOVA, which revealed a significant effect of treatment [11-week-old mice (11W) left, $F_{1,45}=108.26$, $P<0.0001$; 11W right, $F_{1,45}=87.22$, $P<0.0001$; 23-week-old mice (23W) left, $F_{1,8}=28.17$, $P=0.0007$; 23W right, $F_{1,8}=20.57$, $P=0.0019$], but not of genotype effect (11W left, $F_{1,45}=0.24$, $P=0.6301$; 11W right, $F_{1,45}=0.02$, $P=0.8826$; 23W left, $F_{1,8}=4.17$, $P=0.0755$; 23W right, $F_{1,8}=0.57$, $P=0.4714$) and no interaction (11W left, $F_{1,45}=1.72$, $P=0.1963$; 11W right, $F_{1,45}=0.05$, $P=0.8275$; 23W left, $F_{1,8}=1.50$, $P=0.2555$; 23W right, $F_{1,8}=0.00$, $P=1.0000$) (Fig. 2C, D). Finally, the blood corticosterone levels in the groups with short-term chronic stress tended to increase (Supplementary Fig. 3). These results demonstrate that our short-term (3 weeks) and long-term (15 weeks) CIRS protocols can efficiently induce typical physical stress symptoms in mice.

CIRS increases the number of degenerating neurons

Because degenerating neurons appear in L/V-Tg mice without stress after 6 months of age (Chui et al., 1999), the obliteration of neuronal function in the neural circuit involved in cognitive function could be accelerated by the interaction of mutated genes and chronic stress. We thus examined whether stress accelerates neurodegeneration in the L/V-Tg mouse brain by means of the sliver staining: Degenerating neurons were indicated by dense silver precipitates appearing as black grains in their somata (shown by red arrowheads in Fig. 3B) and as cells with numerous fine grains in their somata (shown by red arrowheads in Fig. 3C). On the other hand, typical background signals were indicated by diluted brown particles (shown by a white arrowhead in Fig. 3B). As a result, in L/V-Tg mice degenerating neurons were selectively observed in the circuital areas that correlate with cognitive function. The number of degenerating neurons [% of non-Tg(NS)] was subjected to a two-way ANOVA, which revealed a significant effect of treatment ($F_{1,36}=9.58$, $P=0.0038$), genotype ($F_{1,36}=22.31$, $P<0.0001$), and an interaction ($F_{1,36}=7.18$, $P=0.0110$) in the DG; a significant effect of treatment ($F_{1,28}=8.88$, $P=0.0059$) and genotype ($F_{1,28}=10.13$, $P=0.0036$), but no interaction ($F_{1,28}=1.42$, $P=0.2435$) in the CA3; a significant effect of treatment ($F_{1,32}=25.68$, $P<0.0001$), but not of genotype ($F_{1,32}=2.09$, $P=0.1578$) and interaction ($F_{1,32}=2.19$, $P=0.1487$) in the RCtx; and a significant effect of genotype ($F_{1,27}=8.22$, $P=0.0079$), but not of treatment ($F_{1,27}=1.89$, $P=0.1810$) and interaction ($F_{1,27}=1.07$, $P=0.3108$) in the PCtx (Fig. 3D–G). After short-term CIRS (at 11 weeks of age), the number of degenerating neurons was significantly increased in the DG of L/V-Tg mice [Tukey–Kramer test, $P<0.0001$ vs. non-Tg(NS) and non-Tg(ST); $P<0.001$ vs. L/V-Tg(NS)] (Fig. 3D). The Bonferroni post hoc tests (NS vs. ST) revealed that CIRS increased the number of degenerating neurons in L/V-Tg mice [$P<0.05$, in the CA3 (Fig. 3E); $P<0.001$, in the RCtx (Fig. 3F)]. Especially in the hippocampus of the L/V-Tg(ST) mice, degenerating neurons were drastically increased in the SGZ of the DG, where considerable adult neurogenesis takes place (Fig. 3A). In non-Tg mice, the number of degenerating neurons was slightly increased after short-term CIRS only in the RCtx (Bonferroni test, $P<0.05$, NS vs. ST) (Fig. 3F).

After long-term CIRS (at 23 weeks of age), evidence of neurodegeneration was significantly accumulated in L/V-Tg mice compared with non-Tg mice in various brain regions, including the RCtx and the PCtx (Fig. 4D, E). The number of degenerating neurons was subjected to a two-way ANOVA. This analysis revealed a significant effect of treatment ($F_{1,52}=10.62$, $P=0.0020$), genotype ($F_{1,52}=15.45$, $P=0.0003$), but no interaction ($F_{1,52}=3.38$, $P=0.0719$) in the DG; a significant effect of treatment ($F_{1,44}=7.09$, $P=0.0108$), genotype ($F_{1,44}=19.50$, $P<0.0001$), and an interaction ($F_{1,44}=6.13$, $P=0.0172$) in the CA3; a significant effect of treatment ($F_{1,52}=6.07$,

Fig. 3. The number of degenerating neurons is increased in the brains of stressed animals (short-term). (A) Silver-stained sections of mice exposed to short-term chronic intermittent restraint stress (CIRS) (ST) or left untreated (NS). Scale bar, 100 μm. (B, C) High power pictures of degenerating neurons in the dentate gyrus (DG) (B) and piriform cortex (PCtx) (C) of L/V-Tg(ST) mice (corresponding to the insets in panel A, scale bar, 10 μm). Degenerating neurons are indicated by red arrowheads (B, C); typical background signal is indicated by a white arrowhead (B). (D–G) Graphs indicate the number of degenerating neurons [expressed as % of non-Tg(NS), mean ± SEM] in the DG (D), Cornus Ammonis 3 (CA3) (E), retrosplenial cortex (RCtx) (F), and PCtx (G). Statistical significance; DG [Tukey–Kramer test, ***$P<0.0001$ vs. non-Tg(NS); ###$P<0.0001$ vs. non-Tg(ST); @@$P<0.001$ vs. L/V-Tg (NS)] (D); CA3 (Bonferroni, NS vs. ST, @$P<0.05$) (E); RCtx (Bonferroni, NS vs. ST, #$P<0.05$; @@$P<0.001$) (F). Note that most degenerating neurons in the DG of L/V-Tg(ST) mice are located in the SGZ. Non-Tg, transgenic negative mouse; L/V-Tg, transgenic mouse model of AD with overexpression of an FAD-type PS1; 11W, 11-week-old mice.

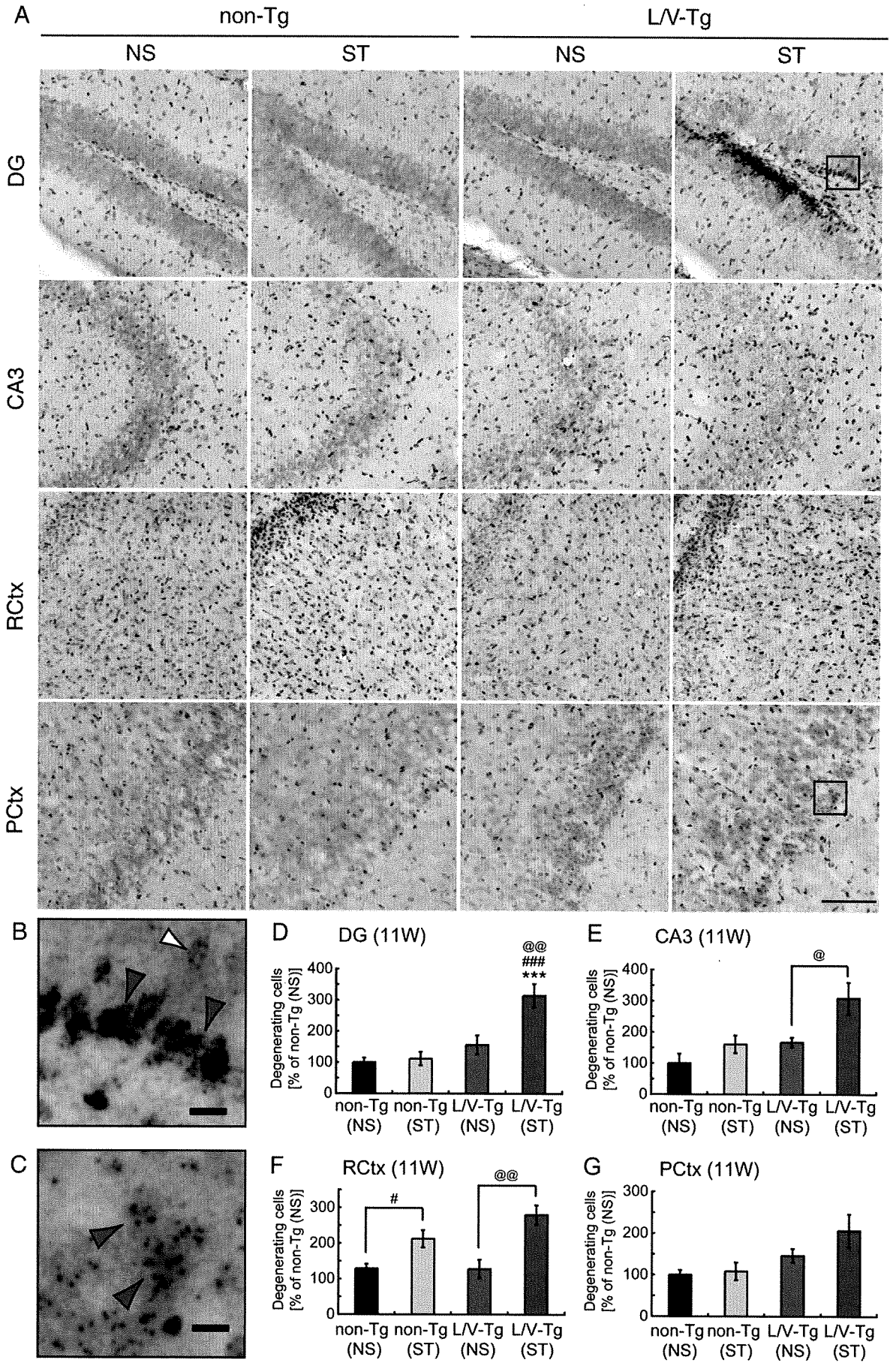
A
non-Tg
L/V-Tg
NS
ST
NS
ST
DG
CA3
RCtx
PCtx
B
C
D
DG (11W)
@@
###
***
Degenerating cells [% of non-Tg (NS)]
400
300
200
100
0
non-Tg (NS)
non-Tg (ST)
L/V-Tg (NS)
L/V-Tg (ST)
E
CA3 (11W)
@
F
RCtx (11W)
#
@@
G
PCtx (11W)

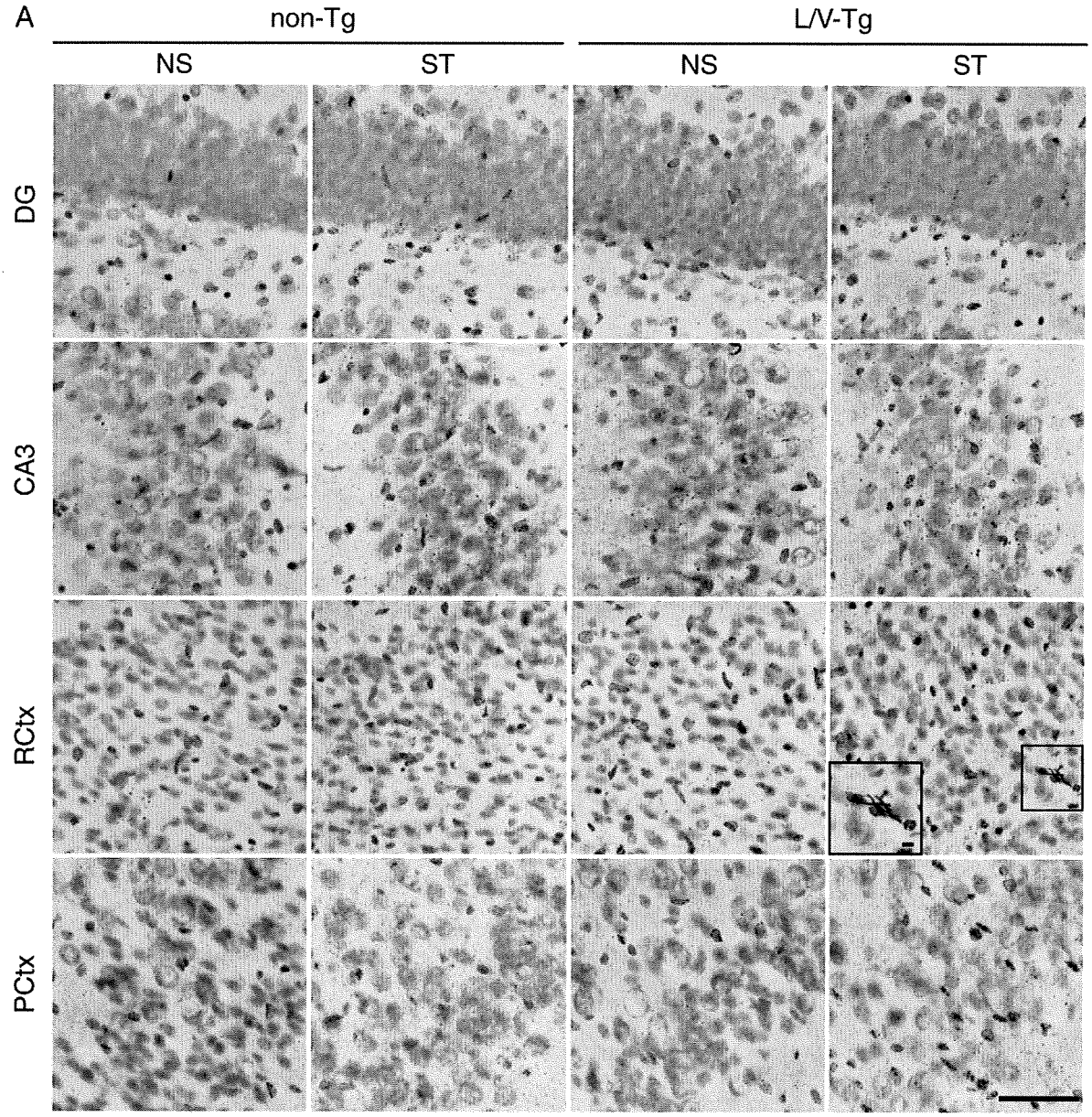
A
non-Tg
L/V-Tg
NS
ST
NS
ST
DG
CA3
RCtx
PCtx

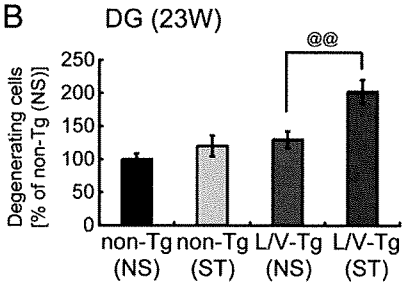
B
DG (23W)
@@
Degenerating cells [% of non-Tg (NS)]
250
200
150
100
50
0
non-Tg (NS)
non-Tg (ST)
L/V-Tg (NS)
L/V-Tg (ST)

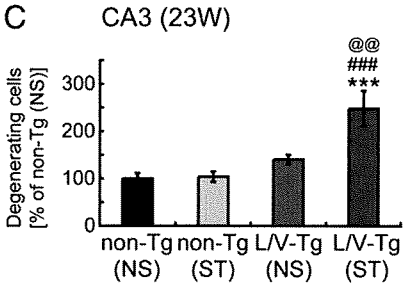
C
CA3 (23W)
@@
###
***
Degenerating cells [% of non-Tg (NS)]
300
200
100
0
non-Tg (NS)
non-Tg (ST)
L/V-Tg (NS)
L/V-Tg (ST)

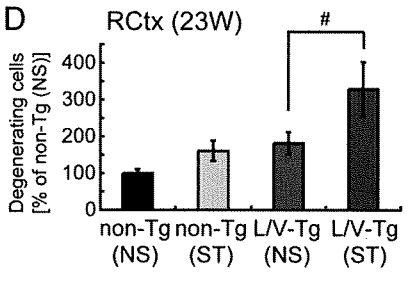
D
RCtx (23W)
#
Degenerating cells [% of non-Tg (NS)]
400
300
200
100
0
non-Tg (NS)
non-Tg (ST)
L/V-Tg (NS)
L/V-Tg (ST)

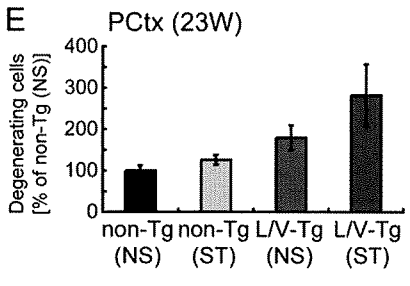
E
PCtx (23W)
Degenerating cells [% of non-Tg (NS)]
400
300
200
100
0
non-Tg (NS)
non-Tg (ST)
L/V-Tg (NS)
L/V-Tg (ST)

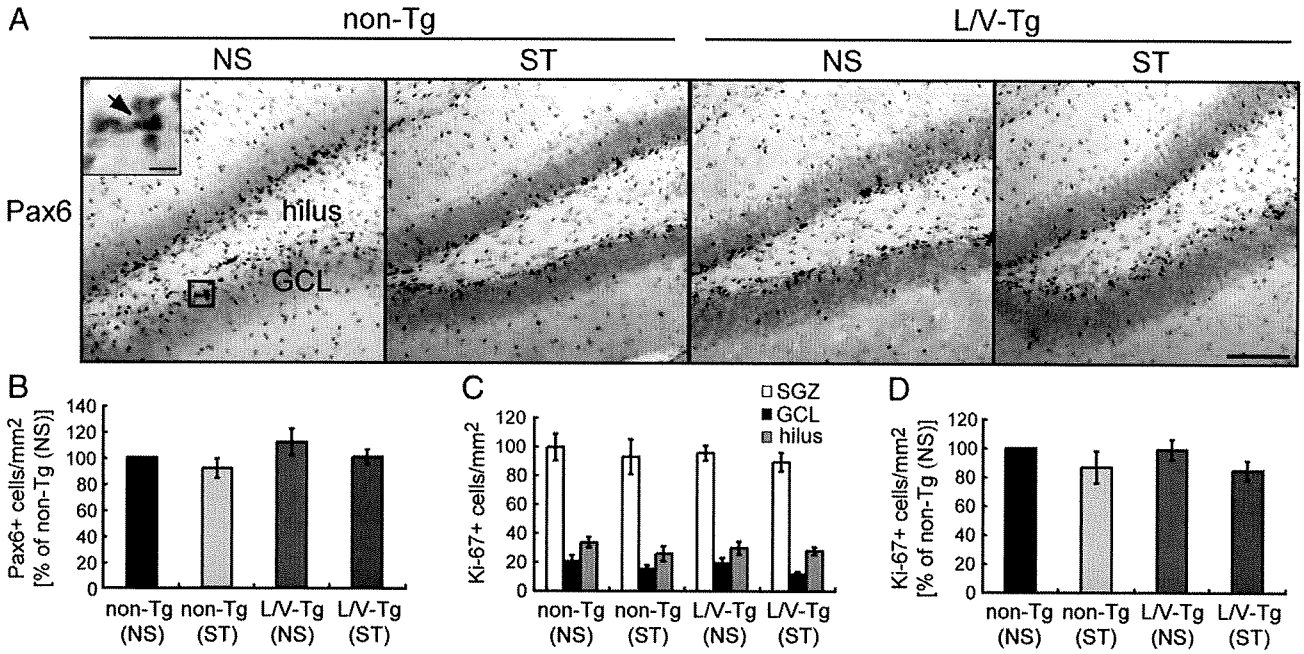

Fig. 5. Short-term chronic intermittent restraint stress (CIRS) slightly affects the number of granule neuron precursors and proliferating cells in the dentate gyrus. (A) Representative immunostaining of Pax6. Scale bar, 50 μm. Inset shows boxed region with a higher magnification (scale bar, 10 μm). An arrow indicates a Pax6+ cell. (B) The number of Pax6+ cells in the subgranular zone (SGZ) [mean ± SEM, % of non-Tg(NS)] tended to decrease in stressed (ST) animals. (C) The number of Ki-67+ cells in each hippocampal region [SGZ, hilus, and granule cell layer (GCL)]. Most Ki-67+ cells are observed in the SGZ, with considerable numbers localized to the hilar region and a few in the GCL. (D) The number of Ki-67+ cells in the GCL and SGZ is slightly decreased to a similar extent in non-Tg and L/V-Tg mice [mean ± SEM, % of non-Tg(NS)]. Non-Tg, transgenic negative mouse; L/V-Tg, transgenic mouse model of AD with overexpression of an FAD-type PS1.

$P=0.0171$) and genotype ($F_{1,52}=8.81$, $P=0.0045$), but no interaction ($F_{1,52}=1.04$, $P=0.3117$) in the RCtx; and a significant effect of genotype ($F_{1,52}=8.19$, $P=0.0061$), but not of treatment ($F_{1,52}=2.45$, $P=0.1237$) and interaction ($F_{1,52}=0.87$, $P=0.3560$) in the PCtx (Fig. 4B–E). The Bonferroni post hoc test (NS vs. ST) found that long-term CIRS significantly increased the number of degenerating cells in L/V-Tg mice [$P<0.01$, in the DG (Fig. 4B); $P<0.05$, in the RCtx (Fig. 4D)]. Multiple comparisons with the Tukey–Kramer test found a significant increase in the number of degenerating neurons in the CA3 of the L/V-Tg(ST) mice [$P<0.0001$ vs. non-Tg(NS) and non-Tg(ST); $P<0.001$ vs. L/V-Tg(NS)] (Fig. 4C).

CIRS with pathogenic PS1 slightly affects the granule neuron precursors and proliferating cells

In stressed L/V-Tg mice, the number of degenerating neurons was significantly increased in the SGZ, where adult neurogenesis occurs. To examine the effect of stress with or without pathogenic PS1 on hippocampal neurogenesis, we next evaluated the number of Pax6+ in the hippocampus of L/V-Tg and non-Tg mice using our short-term CIRS protocol. Adult neurogenesis is an individualized, entire multi-step process but not a population event (Kempermann et al., 2004). Pax6, an essential transcription factor required for the production and maintenance of neural progenitor cells (Maekawa et al., 2005), is expressed in lineage-determined neuronal progenitors, differentiating granule neurons and bipotential (neural) precursor cells, and is strongly down-regulated during granule neuron differentiation (Nacher et al., 2005). In the adult hippocampal DG, proliferating granule neuron precursors that express GFAP and nestin molecules are always Pax6+ (Hevner et al., 2006; Maekawa et al., 2005; Nacher et al., 2005). Thus, Pax6 recently has been used as a suitable marker for newly generated cells (Osumi et al., 2008; von Bohlen Und Halbach, 2007; Winner et al., 2009). Whereas a small subpopulation of hilar mature neurons and certain astrocytes of the adult hippocampus express Pax6, Pax6+ cells in the SGZ are mostly granule neuron precursors (Nacher et al., 2005). Therefore, to evaluate the number of granule neuron precursors, we counted the cells expressing Pax6 localized in the SGZ where considerable new cell production occurs. We found that most Pax6+ cells were in the SGZ (Fig. 5A) and the number of these cells [% of non-Tg(NS)] tended to decrease in non-Tg (ST) and L/V-Tg(ST) mice (Fig. 5B). Yet, a two-way ANOVA revealed no significant effect of treatment ($F_{1,16}=2.04$, $P=0.1720$), genotype ($F_{1,16}=2.31$, $P=0.1479$), or interaction ($F_{1,16}=0.05$, $P=0.8203$). Consequently, we found that neither 3 weeks of CIRS (short-term) nor the PS1(L286V) genotype greatly affects the number of granule neuron precursors in the SGZ.

Granule neuron precursors are born in the SGZ and a neural precursor produces a bipotential neural cell and a lineage-determined neuronal cell through asymmetric division (Kempermann et al., 2004). We also measured the number of Ki-67+ cells per GCL to evaluate the proliferating cells. Ki-67 is present only in proliferating cells during G1, S, G2, and M, but not in the G0 phase of the cell cycle (Brown and Gatter, 1990; Kee et al., 2002). The number of Ki-67+ cells was subjected to a two-way ANOVA, which showed no significant effect of genotype [$F_{1,22}=0.18$, $P=0.6758$ (SGZ); $F_{1,22}=0.03$, $P=0.8705$ (hilus); $F_{1,22}=0.54$, $P=0.4710$ (GCL)], treatment [$F_{1,22}=0.61$, $P=0.4442$ (SGZ); $F_{1,22}=1.32$, $P=0.2631$ (hilus); $F_{1,22}=3.63$, $P=0.0700$ (GCL)], or interaction [$F_{1,22}=0.00$, $P=0.9901$ (SGZ); $F_{1,22}=0.60$, $P=0.4481$ (hilus); $F_{1,22}=0.12$, $P=0.7277$ (GCL)] (Fig. 5C). The percentage of Ki-67+ cells in the GCL and SGZ also

Fig. 4. The number of degenerating neurons is increased in the brains of stressed animals (long-term). (A) Silver-stained sections of mice exposed to chronic intermittent restraint stress (CIRS) (ST) or left untreated (NS). Scale bar, 100 μm. Inset shows boxed regions with higher magnification (scale bar, 10 μm). (B–E) Graphs indicate the number of degenerating neurons [expressed as % of non-Tg(NS), mean ± SEM] in the dentate gyrus (DG) (B), Cornus Ammonis 3 (CA3) (C), retrosplenial cortex (RCtx) (D), and piriform cortex (PCtx) (E). Statistical significance; DG (Bonferroni, NS vs. ST, @@$P<0.01$) (B); CA3 [Tukey–Kramer test, ***$P<0.0001$ vs. non-Tg(NS); ###$P<0.0001$ vs. non-Tg(ST); @@$P<0.001$ vs. L/V-Tg(NS)] (C); RCtx (Bonferroni, NS vs. ST, #$P<0.05$) (D). Non-Tg, transgenic negative mouse; L/V-Tg, transgenic mouse model of AD with overexpression of an FAD-type PS1; 23W, 23-week-old mice.

showed no significant effect of genotype ($F_{1,22}=0.05$, $P=0.8247$) or treatment ($F_{1,22}=3.84$, $P=0.0629$) or an interaction ($F_{1,22}=0.01$, $P=0.9205$). As a result, 3 weeks of CIRS slightly decreased the number of Ki-67+ proliferating cells in the SGZ, hilus, and GCL to a similar extent in non-Tg and L/V-Tg mice (Fig. 5C, D). In short, we confirmed that short-term CIRS primarily decreased the production of granule neuron precursors and the number of proliferating cells in the GCL and SGZ, yet the effect did not show significant differences between non-Tg and L/V-Tg backgrounds.

The impact of CIRS on newly synthesized cells lasts longer in Tg than in Non-Tg

In order to quantify the rate of neural production in the GCL and SGZ after stress exposure, we counted the newly synthesized cells by a single intraperitoneal injection of BrdU 20 h before perfusion. Unlike the measurement of the Pax6+ granule neuron precursors that integrates all of the marker-positive cells produced during the whole experimental (stressed/non-stressed) period, this BrdU labeling protocol can estimate only those cells newly synthesized within a day after stress cessation. When using Ki-67 to quantify the cell proliferation, newly generated cells that exit the cell cycle and enter their maturation process are not detected. BrdU is incorporated in cells at the S-phase, allowing us to detect both mitotic cells (Type-1, Type-2a, 2b, Type-3) and postmitotic cells (including late Type-3) in the hippocampal DG [the classification of the cellular stage in neurogenesis was performed in accordance with the review by Kempermann (Kempermann et al., 2004)] by immunohistochemical analyses using an anti-BrdU antibody. Actually, in adult hippocampal neurogenesis of mice, one can find a considerable number of cells labeled for both BrdU and NeuN (a post-mitotic, neuronal cell marker) even 1 day after a single injection of BrdU (Brandt et al., 2003). The number of BrdU+ cells in the GCL and SGZ [% of non-Tg(NS)] was subjected to a two-way ANOVA, and this analysis did show a significant effect of treatment ($F_{1,15}=24.12$, $P=0.0002$), but no effect of genotype ($F_{1,15}=2.06$, $P=0.1716$) and interaction ($F_{1,15}=1.78$, $P=0.2026$). Bonferroni *post hoc* tests (NS vs. ST) revealed that after CIRS, the number of BrdU+ cells was significantly reduced in L/V-Tg mice ($P<0.001$) [63 ± 7% of BrdU + cells in non-Tg(NS), Fig. 6A, B] but was not significantly decreased in non-Tg mice ($P>0.05$) [79 ± 9% of BrdU+ cells in non-Tg(NS), Fig. 6A, B]. This trend was almost parallel with the pattern in the body-weight-gain reductions (Supplementary Table 1). These results indicate that the impact of stress on newly synthesized cells in L/V-Tg mice lasted longer than that in non-Tg mice.

DCX+ neuronal progenitor cells increased after CIRS only in Tg

Although the significant reduction in the number of BrdU+ newly synthesized cells at 20 h after stress in L/V-Tg mice was apparent, the number of Pax6+ granule neuron precursors in the SGZ and Ki-67+ proliferating cells in the GCL and SGZ did not significantly decrease during the short-term CIRS. In hippocampal neurogenesis, a dividing precursor cell gives rise to daughter cells, which migrate away from the site of division and start to differentiate into neurons (Kempermann et al., 2004). We therefore evaluated the effect of short-term CIRS on the neuronal progenitor cells in the GCL and SGZ using the microtubule-associated protein doublecortin (DCX) as a marker. DCX is normally retained in cells within areas of continuous neurogenesis and expressed in mitotic and postmitotic cells (Brown et al., 2003; Couillard-Despres et al., 2005; Rao and Shetty, 2004), namely, proliferative nestin-positive neuronal progenitor cells (Type-2b), nestin-negative neuronal progenitor cells (Type-3), and postmitotic immature neurons that retain the vertical morphology with a rounded or slightly triangular nucleus and a clearly visible apical dendrite (late Type-3) (Kempermann et al., 2004). As the

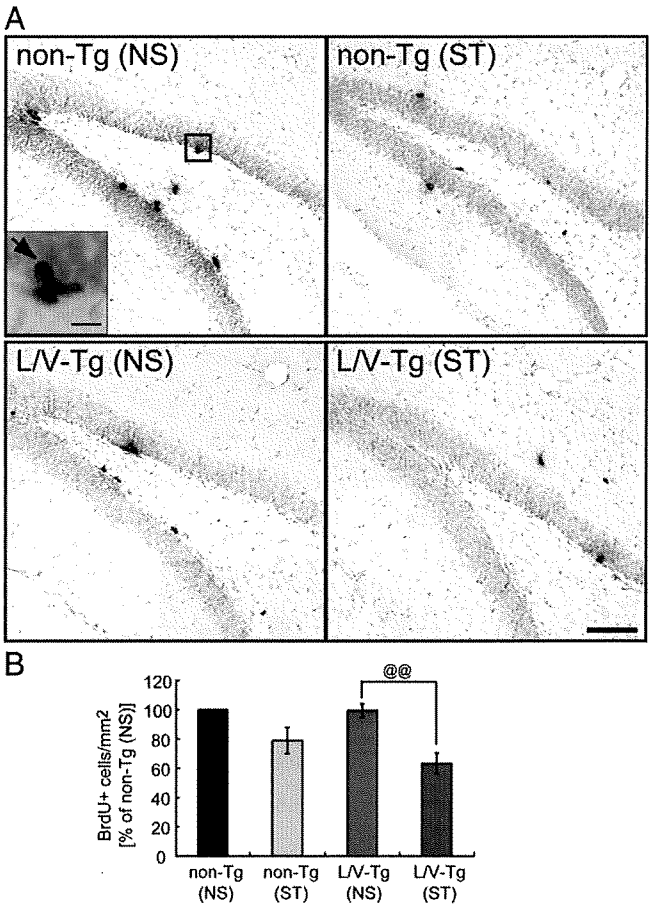

Fig. 6. The impact of chronic intermittent restraint stress (CIRS) on newly synthesized cells in the granule cell layer (GCL) and the subgranular zone (SGZ) lasts longer in L/V-Tg mice than in non-Tg mice. (A) Representative immunostaining of 5-bromo-2′-deoxyuridine (BrdU)+ cells. Scale bar, 50 μm. Inset shows boxed region with a higher magnification (scale bar, 10 μm). An arrow indicates a BrdU+ cell. (B) After CIRS, the number of BrdU+ cells in the GCL and SGZ [mean ± SEM, % of non-Tg(NS)] is significantly reduced in L/V-Tg mice (Bonferroni, NS vs. ST, @@$P<0.001$) but is not significantly decreased in non-Tg mice. Non-Tg, transgenic negative mouse; L/V-Tg, transgenic mouse model of AD with overexpression of an FAD-type PS1; NS, non-stressed control mice; ST, stressed mice.

newly generated cells began expressing mature neuronal markers, DCX immunoreactivity decreased sharply below the level of detection and remained undetectable thereafter (Brown et al., 2003; Couillard-Despres et al., 2005; Rao and Shetty, 2004). The number of DCX+ cells in the GCL and SGZ [% of non-Tg(NS)] was subjected to a two-way ANOVA, and this analysis showed a significant effect of treatment ($F_{1,30}=5.48$, $P=0.0261$) and an interaction ($F_{1,30}=23.37$, $P<0.0001$), but no effect of genotype ($F_{1,30}=1.76$, $P=0.1943$). Tukey-Kramer post hoc tests revealed significant differences in the number of DCX+ progenitor cells in the GCL and SGZ. In stressed non-Tg mice, the number of DCX+ cells significantly reduced [$P<0.0001$ vs. non-Tg(NS)] (Fig. 7A, B). This is in agreement with the trends observed for the Pax6+, Ki-67+, and BrdU+ cells. On the other hand, in L/V-Tg mice, the number of DCX+ cells was significantly reduced without stress [78 ± 2 % of DCX+ cells in non-Tg(NS); $P<0.0001$ vs. non-Tg(NS), Fig. 7B]. Unexpectedly, in L/V-Tg mice, the number of DCX+ neuronal progenitors was significantly increased by short-term CIRS [12 % increase compared with non-stressed L/V-Tg; $P<0.001$ vs. L/V-Tg(NS), Fig. 7B]. Equivalent data were obtained from confocal laser scanning microscopic analyses of the doublecortin (DCX)+ neuronal progenitor cells in the GCL and SGZ (Supplementary Fig. 4). Additionally, in the stressed L/V-Tg mice, the percentage of DCX+ cells that possessed long neurites (late

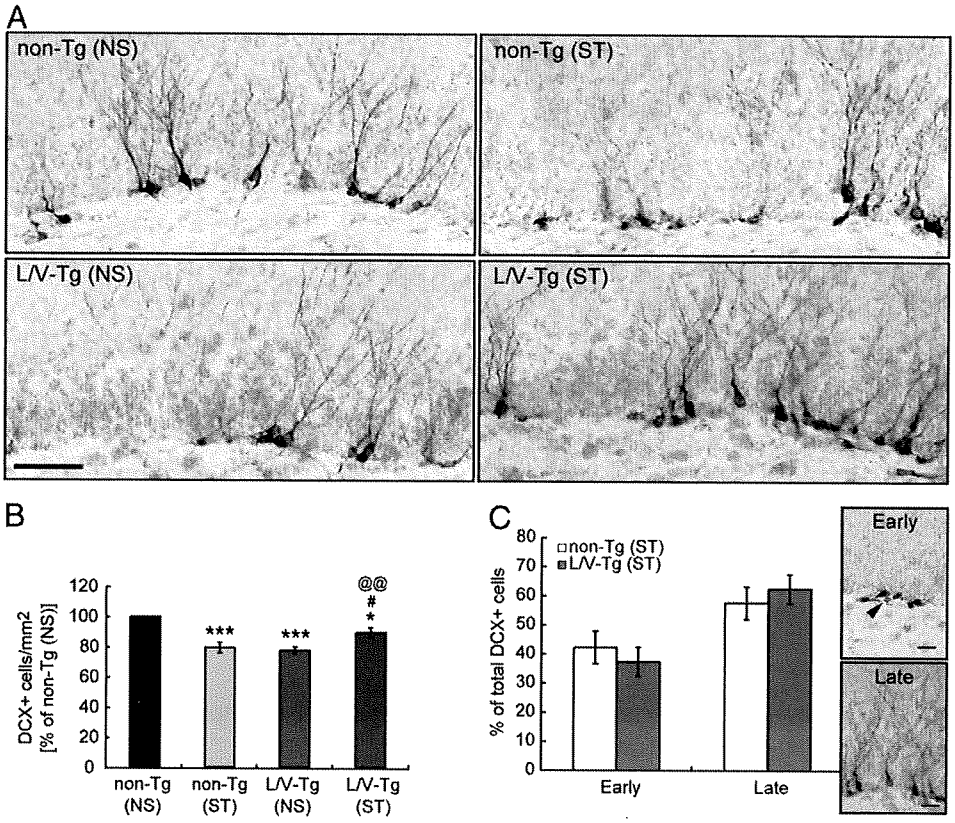

Fig. 7. Neuronal progenitor cells in the granule cell layer (GCL) and the subgranular zone (SGZ) increase after chronic intermittent restraint stress (CIRS) only in Tg. (A) Representative immunostaining of the doublecortin (DCX)+ neuronal progenitor cells in the GCL and SGZ. Scale bar, 50 μm. (B) The DCX+ cells in the GCL and SGZ [mean ± SEM, % of non-Tg(NS)] are significantly reduced in non-stressed L/V-Tg mice and are increased in stressed L/V-Tg mice. *$P<0.05$, ***$P<0.0001$ vs. non-Tg(NS); #$P<0.05$ vs. non-Tg(ST); @@$P<0.001$ vs. L/V-Tg(NS) (Tukey–Kramer test). (C) The percentage of DCX+ cells that possessed short neurites (Early, early progenitor cells) or long neurites (Late, late progenitor cells) in non-Tg(ST) and L/V-Tg(ST) mice (mean ± SEM). Scale bar, 50 μm. DCX+ late progenitor cells are modestly increased in L/V-Tg(ST) mice compared with non-Tg(ST) mice. Non-Tg, transgenic negative mouse; L/V-Tg, transgenic mouse model of AD with overexpression of an FAD-type PS1; NS, non-stressed control mice; ST, stressed mice.

progenitor cells) was modestly increased over that of non-Tg mice, whereas early progenitor cells tended to decrease compared with that of non-Tg mice (Fig. 7C).

Discussion

Our study indicates how gene–environment interaction affects adult neurogenesis in the hippocampal DG and deteriorates selective neurodegeneration in the neuronal circuit involved in cognitive function. We speculate that, in genetically predisposed animals, accumulated effects of subtle daily stresses such as metabolic oxidation may cause neurodegeneration, even in the absence of environmental stress.

Cellular and molecular machineries that accelerate neurodegeneration by chronic stress

Neurodegeneration in stressed L/V-Tg mice was more severe than in stressed non-Tg mice (Fig. 3). This might be due to increased vulnerability at the cellular or system levels, which is supported by our observation of abnormal calcium homeostasis in primary cultured hippocampal neurons prepared from neonatal L/V-Tg mice (data not shown). A previous report indicated that the PS1(L286V) mutation lowers the threshold to neurotoxicity through the disruption of calcium homeostasis and increased free radical production (Grilli et al., 2000; Guo et al., 1997). While structural changes after stress are often found in the CA3 (Conrad, 2006), we found that neurodegeneration in the stressed L/V-Tg mice was most prominent in the SGZ of the DG, where adult neurogenesis occurs. Because PS1 plays a role in neurogenesis both during development and in the adult (Wen et al., 2002), neurogenesis in the SGZ could be affected by chronic stress more than that in non-Tg mice.

In L/V-Tg mice, the number of DCX+ neuronal progenitors in the GCL and SGZ was significantly reduced without stress (Fig. 7A, B). This is in accord with recent evidence demonstrating that an FAD-related homozygous PS1 P264L mutation resulted in decreased numbers of DCX+ cells in the GCL (Zhang et al., 2007). On the other hand, the number of DCX+ cells in the GCL was significantly increased by short-term CIRS (Fig. 7A, B), which is consistent with the observation that the number of DCX+ cells in the hippocampal GCL increases in a senile cohort of AD patients (Jin et al., 2004). Another recent publication shows that increased proliferating cells in the presenile AD hippocampus are mostly accounted for by glial and vascular-associated changes, but not by neurogenesis (Boekhoorn et al., 2006). These contradictions can be attributed to multiple factors, such as different phases of AD progression, animal models, methodologies, and analytical tools (Kuhn et al., 2007). In our study, both decreased and increased states of DCX+ cells were driven in the L/V-Tg mice using the chronic stress model. These mice would therefore contribute to unravelling the aberrant neurogenic/nonneurogenic mechanisms that are part of the pathological events of neurodegenerative diseases.

Despite increased numbers of DCX+ cells in the GCL of AD patients (Jin et al., 2004) and short-term chronically stressed L/V-Tg mice, progressive neurodegeneration was still observed after long-term CIRS, implicating that the repair capacity of the DCX+ cells in the GCL is limited. Notably, the number of BrdU+ newly synthesized cells was significantly reduced in the GCL and SGZ (Fig. 6A, B). Considering the fact that BrdU+ cells contain both neural and neuronal fate cells (Maekawa et al., 2005), together with the observation that production of Pax6+ granule neuron precursors in the SGZ reached a similar

extent in stressed non-Tg and L/V-Tg mice, cells with a neuronal fate might preferentially be reduced in 20 h after CIRS. In stressed L/V-Tg mice, percentage of postmitotic DCX+ cells possessing longer neurites (late Type-3) was modestly increased compared with that in non-Tg (ST) mice, whereas the number of mitotic DCX+ cells (Type-2b and early Type-3) tended to decrease compared with that of non-Tg(ST) mice (Fig. 7C). This indicates that numerous DCX+ neuronal progenitor cells observed in the GCL and SGZ of stressed L/V-Tg mice were late-stage (posmitotic late Type-3), rather than early-stage (mitotic Type-2b and Type-3), in neuronal maturation. Collectively, these data suggest that an interaction between pathogenic PS1 and CIRS does affect neurogenesis during postmitotic neuronal cell maturation. We reasoned that the elevated number of DCX+ cells in the GCL and SGZ of stressed L/V-Tg mice was derived from an accumulation of immature neuronal progenitor cells rather than a replenishment of granule cells. A recent report indicated that DCX molecule supports dendritic arborization (Cohen et al., 2008). Given that DCX+ cells were accumulated in the GCL of stressed L/V-Tg mice, abnormal DCX degradation and consequent excessive stabilization of microtubules by DCX could in part explain the retardation of neuronal maturation and the resultant neurodegeneration. PS1 mutations might synergistically affect the expression, processing, or trafficking of molecules essential to neuronal maturation, such as Wnts, BDNF, and Trk receptors (Naruse et al., 1998), although further molecular–cellular assessment would be needed.

From a therapeutic point of view, it is necessary to elucidate the detailed molecular machinery that perturbs granule cell maturation and neurodegeneration in the hippocampal DG. The ability to recover from stress-related impaired neurogenesis, which was shown in wild-type adult rats (Heine et al., 2004), would be unbalanced presumably by the vulnerability derived from the mutated gene–chronic stress interaction in stressed L/V-Tg mice. For instance, under the stressed condition, apoptosis machinery is not available in L/V-Tg mice to actively eliminate those cells in abnormal neuronal differentiation, resulting in an accumulation of ill-balanced neurodegenerative cells in the hippocampus, even at the younger stages. This is partly supported by our observation that the number of TUNEL-positive apoptotic cells in the GCL did not significantly fluctuate between L/V-Tg and wild-type mice with CIRS (Supplementary Fig. 5), and the phenotype might further be strengthened by the fact that the number of newly synthesized cells assessed by BrdU was 33% decreased in L/V-Tg(ST) mice (Fig. 6). A non-cell autonomous microenvironmental niche induced by FAD-linked PS1 variants could be additionally responsible for the impaired neurogenesis and neurodegeneration (Choi et al., 2008).

Conclusions

Our results suggest that, in individuals predisposed to genetic mutations for AD, stress accelerates the inhibition of neuronal maturation, thereby enhancing neurodegenerative vulnerability that depends on mutated gene–environment interaction. Chronically stressed L/V-Tg mice could be useful animal models to elucidate the key molecular machinery and therapeutic targets for AD. Our experimental strategy using controlled stress should provide insights into the pathogenic mechanisms of AD as well as other neurodegenerative diseases.

Acknowledgments

We thank Drs. S. Kohsaka and M. Hoshino for their help, Ms. T. Kohno and J. Asami for technical assistance and all other members of the Shindan, DDND and DVDR lab for fruitful discussions. We also thank Drs. H. Kumanogoh, R. Setsuie, K. Zushida, T. Maruoka, M. Yokosuka, K. Yuyama, T. Kikusui, and K. Moriya for providing useful information. This work was supported by a Grant-in-Aid for Young Scientists (B) (#18790607; #21790639) to S.K., grants from Research Foundation ITSUU Laboratory and Takeda Science Foundation to T.I., and the Program for Promotion of Fundamental Studies in Health Sciences of the National Institute of Biomedical Innovation (05-32) to S. N., K. W. and T. I.

Appendix A. Supplementary data

Supplementary data associated with this article can be found, in the online version, at doi:10.1016/j.expneurol.2009.10.020.

References

Boekhoorn, K., Joels, M., Lucassen, P.J., 2006. Increased proliferation reflects glial and vascular-associated changes, but not neurogenesis in the presenile Alzheimer hippocampus. Neurobiol. Dis. 24, 1–14.
Brandt, M.D., Jessberger, S., Steiner, B., Kronenberg, G., Reuter, K., Bick-Sander, A., von der Behrens, W., Kempermann, G., 2003. Transient calretinin expression defines early postmitotic step of neuronal differentiation in adult hippocampal neurogenesis of mice. Mol. Cell. Neurosci. 24, 603–613.
Brown, D.C., Gatter, K.C., 1990. Monoclonal antibody Ki-67: its use in histopathology. Histopathology 17, 489–503.
Brown, J.P., Couillard-Després, S., Cooper-Kuhn, C.M., Winkler, J., Aigner, L., Kuhn, H.G., 2003. Transient expression of doublecortin during adult neurogenesis. J. Comp. Neurol. 467, 1–10.
Bruel-Jungerman, E., Laroche, S., Rampon, C., 2005. New neurons in the dentate gyrus are involved in the expression of enhanced long-term memory following environmental enrichment. Eur. J. Neurosci. 21, 513–521.
Buckner, R.L., 2004. Memory and executive function in aging and AD: multiple factors that cause decline and reserve factors that compensate. Neuron 44, 195–208.
Cameron, H.A., McKay, R.D., 2001. Adult neurogenesis produces a large pool of new granule cells in the dentate gyrus. J. Comp. Neurol. 435, 406–417.
Choi, S.H., Veeraraghavalu, K., Lazarov, O., Marler, S., Ransohoff, R.M., Ramirez, J.M., Sisodia, S.S., 2008. Non-cell-autonomous effects of presenilin 1 variants on enrichment-mediated hippocampal progenitor cell proliferation and differentiation. Neuron 59, 568–580.
Chui, D.H., Tanahashi, H., Ozawa, K., Ikeda, S., Checler, F., Ueda, O., Suzuki, H., Araki, W., Inoue, H., Shirotani, K., Takahashi, K., Gallyas, F., Tabira, T., 1999. Transgenic mice with Alzheimer presenilin 1 mutations show accelerated neurodegeneration without amyloid plaque formation. Nat. Med. 5, 560–564.
Cohen, D., Segal, M., Reiner, O., 2008. Doublecortin supports the development of dendritic arbors in primary hippocampal neurons. Dev. Neurosci. 30, 187–199.
Conrad, C.D., 2006. What is the functional significance of chronic stress-induced CA3 dendritic retraction within the hippocampus? Behav. Cogn. Neurosci. Rev. 5, 41–60.
Couillard-Despres, S., Winner, B., Schaubeck, S., Aigner, R., Vroemen, M., Weidner, N., Bogdahn, U., Winkler, J., Kuhn, H.G., Aigner, L., 2005. Doublecortin expression levels in adult brain reflect neurogenesis. Eur. J. Neurosci. 21, 1–14.
Drapeau, E., Mayo, W., Aurousseau, C., Le Moal, M., Piazza, P.V., Abrous, D.N., 2003. Spatial memory performances of aged rats in the water maze predict levels of hippocampal neurogenesis. Proc. Natl. Acad. Sci. U. S. A. 100, 14385–14390.
Golde, T.E., Eckman, C.B., Younkin, S.G., 2000. Biochemical detection of Abeta isoforms: implications for pathogenesis, diagnosis, and treatment of Alzheimer's disease. Biochim. Biophys. Acta 1502, 172–187.
Gould, E., Tanapat, P., 1999. Stress and hippocampal neurogenesis. Biol. Psychiatry 46, 1472–1479.
Gould, E., Beylin, A., Tanapat, P., Reeves, A., Shors, T.J., 1999. Learning enhances adult neurogenesis in the hippocampal formation. Nat. Neurosci. 2, 260–265.
Grilli, M., Diodato, E., Lozza, G., Brusa, R., Casarini, M., Uberti, D., Rozmahel, R., Westaway, D., St George-Hyslop, P., Memo, M., Ongini, E., 2000. Presenilin-1 regulates the neuronal threshold to excitotoxicity both physiologically and pathologically. Proc. Natl. Acad. Sci. U. S. A. 97, 12822–12827.
Guo, Q., Sopher, B.L., Furukawa, K., Pham, D.G., Robinson, N., Martin, G.M., Mattson, M.P., 1997. Alzheimer's presenilin mutation sensitizes neural cells to apoptosis induced by trophic factor withdrawal and amyloid beta-peptide: involvement of calcium and oxyradicals. J. Neurosci. 17, 4212–4222.
Heine, V.M., Maslam, S., Zareno, J., Joëls, M., Lucassen, P.J., 2004. Suppressed proliferation and apoptotic changes in the rat dentate gyrus after acute and chronic stress are reversible. Eur. J. Neurosci. 19, 131–144.
Hevner, R.F., Hodge, R.D., Daza, R.A., Englund, C., 2006. Transcription factors in glutamatergic neurogenesis: conserved programs in neocortex, cerebellum, and adult hippocampus. Neurosci. Res. 55, 223–233.
Imayoshi, I., Sakamoto, M., Ohtsuka, T., Takao, K., Miyakawa, T., Yamaguchi, M., Mori, K., Ikeda, T., Itohara, S., Kageyama, R., 2008. Roles of continuous neurogenesis in the structural and functional integrity of the adult forebrain. Nat. Neurosci. 11, 1153–1161.
Ino, H., 2003. Antigen retrieval by heating en bloc for pre-fixed frozen material. J. Histochem. Cytochem. 51, 995–1003.
Inoue, T., Nakamura, S., Osumi, N., 2000. Fate mapping of the mouse prosencephalic neural plate. Dev. Biol. 219, 373–383.
Jack Jr., C.R., Petersen, R.C., O'Brien, P.C., Tangalos, E.G., 1992. MR-based hippocampal volumetry in the diagnosis of Alzheimer's disease. Neurology 42, 183–188.
Jeong, Y.H., Park, C.H., Yoo, J., Shin, K.Y., Ahn, S.M., Kim, H.S., Lee, S.H., Emson, P.C., Suh, Y.H., 2006. Chronic stress accelerates learning and memory impairments and increases

amyloid deposition in APPV717I-CT100 transgenic mice, an Alzheimer's disease model. FASEB J. 20, 729–731.
Jin, K., Peel, A.L., Mao, X.O., Xie, L., Cottrell, B.A., Henshall, D.C., Greenberg, D.A., 2004. Increased hippocampal neurogenesis in Alzheimer's disease. Proc. Natl. Acad. Sci. U. S. A. 101, 343–347.
Kee, N., Sivalingam, S., Boonstra, R., Wojtowicz, J.M., 2002. The utility of Ki-67 and BrdU as proliferative markers of adult neurogenesis. J. Neurosci. Methods 115, 97–105.
Kempermann, G., Gage, F.H., 2002. Genetic determinants of adult hippocampal neurogenesis correlate with acquisition, but not probe trial performance, in the water maze task. Eur. J. Neurosci. 16, 129–136.
Kempermann, G., Jessberger, S., Steiner, B., Kronenberg, G., 2004. Milestones of neuronal development in the adult hippocampus. Trends Neurosci. 27, 447–452.
Killiany, R.J., Moss, M.B., Albert, M.S., Sandor, T., Tieman, J., Jolesz, F., 1993. Temporal lobe regions on magnetic resonance imaging identify patients with early Alzheimer's disease. Arch. Neurol. 50, 949–954.
Kim, K.S., Han, P.L., 2006. Optimization of chronic stress paradigms using anxiety- and depression-like behavioral parameters. J. Neurosci. Res. 83, 497–507.
Kuhn, H.G., Cooper-Kuhn, C.M., Boekhoorn, K., Lucassen, P.J., 2007. Changes in neurogenesis in dementia and Alzheimer mouse models: are they functionally relevant? Eur. Arch. Psychiatry Clin. Neurosci. 257, 281–289.
Maekawa, M., Takashima, N., Arai, Y., Nomura, T., Inokuchi, K., Yuasa, S., Osumi, N., 2005. Pax6 is required for production and maintenance of progenitor cells in postnatal hippocampal neurogenesis. Genes Cells 10, 1001–1014.
Masters, C.L., Beyreuther, K., 1998. Alzheimer's disease. British Med. J. 316, 446–448.
Mattson, M.P., 2004. Pathways towards and away from Alzheimer's disease. Nature 430, 631–639.
Nacher, J., Varea, E., Blasco-Ibañez, J.M., Castillo-Gomez, E., Crespo, C., Martinez-Guijarro, F.J., McEwen, B.S., 2005. Expression of the transcription factor Pax 6 in the adult rat dentate gyrus. J. Neurosci. Res. 81, 753–761.
Nagata, K., Nakashima-Kamimura, N., Mikami, T., Ohsawa, I., Ohta, S., 2009. Consumption of molecular hydrogen prevents the stress-induced impairments in hippocampus-dependent learning tasks during chronic physical restraint in mice. Neuropsychopharmacology 34, 501–508.
Naruse, S., Thinakaran, G., Luo, J.J., Kusiak, J.W., Tomita, T., Iwatsubo, T., Qian, X., Ginty, D.D., Price, D.L., Borchelt, D.R., Wong, P.C., Sisodia, S.S., 1998. Effects of PS1 deficiency on membrane protein trafficking in neurons. Neuron 21, 1213–1221.
Ogita, K., Nishiyama, N., Sugiyama, C., Higuchi, K., Yoneyama, M., Yoneda, Y., 2005. Regeneration of granule neurons after lesioning of hippocampal dentate gyrus: evaluation using adult mice treated with trimethyltin chloride as a model. J. Neurosci. Res. 82, 609–621.
Osumi, N., Shinohara, H., Numayama-Tsuruta, K., Maekawa, M., 2008. Concise review: Pax6 transcription factor contributes to both embryonic and adult neurogenesis as a multifunctional regulator. Stem Cells 26, 1663–1672.
Pardon, M.C., Rattray, I., 2008. What do we know about the long-term consequences of stress on ageing and the progression of age-related neurodegenerative disorders? Neurosci. Biobehav. Rev. 32, 1103–1120.
Paxinos, G., Franklin, K.B., 2001. The Mouse Brain in Stereotaxic Coordinates, 2nd edn. Academic Press, San Diego.
Rao, M.S., Shetty, A.K., 2004. Efficacy of doublecortin as a marker to analyse the absolute number and dendritic growth of newly generated neurons in the adult dentate gyrus. Eur. J. Neurosci. 19, 234–246.
Rosenbrock, H., Koros, E., Bloching, A., Podhorna, J., Borsini, F., 2005. Effect of chronic intermittent restraint stress on hippocampal expression of marker proteins for synaptic plasticity and progenitor cell proliferation in rats. Brain Res. 1040, 55–63.
Sandi, C., 2004. Stress, cognitive impairment and cell adhesion molecules. Nat. Rev. Neurosci. 5, 917–930.
Shors, T.J., Miesegaes, G., Beylin, A., Zhao, M., Rydel, T., Gould, E., 2001. Neurogenesis in the adult is involved in the formation of trace memories. Nature 410, 372–376.
Veena, J., Srikumar, B.N., Mahati, K., Bhagya, V., Raju, T.R., Shankaranarayana Rao, B.S., 2009. Enriched environment restores hippocampal cell proliferation and ameliorates cognitive deficits in chronically stressed rats. J. Neurosci. Res. 87, 831–843.
von Bohlen Und Halbach, O., 2007. Immunohistological markers for staging neurogenesis in adult hippocampus. Cell Tissue Res. 329, 409–420.
Wen, P.H., Friedrich Jr., V.L., Shioi, J., Robakis, N.K., Elder, G.A., 2002. Presenilin-1 is expressed in neural progenitor cells in the hippocampus of adult mice. Neurosci. Lett. 318, 53–56.
Winner, B., Desplats, P., Hagl, C., Klucken, J., Aigner, R., Ploetz, S., Laemke, J., Karl, A., Aigner, L., Masliah, E., Buerger, E., Winkler, J., 2009. Dopamine receptor activation promotes adult neurogenesis in an acute Parkinson model. Exp. Neurol. 219, 543–552.
Zhang, C.L., Zou, Y., He, W., Gage, F.H., Evans, R.M., 2008. A role for adult TLX-positive neural stem cells in learning and behaviour. Nature 451, 1004–1007.
Zhang, C., McNeil, E., Dressler, L., Siman, R., 2007. Long-lasting impairment in hippocampal neurogenesis associated with amyloid deposition in a knock-in mouse model of familial Alzheimer's disease. Exp. Neurol. 204, 77–87.

RESEARCH ARTICLE

AMERICAN JOURNAL OF medical genetics PART B
Neuropsychiatric Genetics

Sexually Dimorphic Effect of the Val66Met Polymorphism of *BDNF* on Susceptibility to Alzheimer's Disease: New Data and Meta-Analysis

Noriko Fukumoto,[1] Takashi Fujii,[2] Onofre Combarros,[3] M. Ilyas Kamboh,[4] Shin-Jen Tsai,[5] Sachio Matsushita,[6] Benedetta Nacmias,[7] David E. Comings,[8] Humberto Arboleda,[9] Martin Ingelsson,[10] Bradley T. Hyman,[11] Hiroyasu Akatsu,[12] Andrew Grupe,[13] Agnes Lumi Nishimura,[14] Mayana Zatz,[14] Kari M. Mattila,[15,16] Juha Rinne,[17] Yu-ichi Goto,[18] Takashi Asada,[19] Shun Nakamura,[1] and Hiroshi Kunugi[2]*

[1]Department of Biochemistry and Cellular Biology, National Institute of Neuroscience, National Center of Neurology and Psychiatry, Kodaira, Tokyo, Japan

[2]Department of Mental Disorder Research, National Institute of Neuroscience, National Center of Neurology and Psychiatry, Kodaira, Tokyo, Japan

[3]Neurology Service, University Hospital 'Marqués de Valdecilla', Santander, Spain

[4]Department of Human Genetics, Graduate School of Public Health, University of Pittsburgh, Pittsburgh, Pennsylvania

[5]Department of Psychiatry, Taipei Veterans General Hospital, Taipei, Taiwan

[6]National Hospital Organization, Kurihama Alcoholism Center, Yokosuka, Kanagawa, Japan

[7]Department of Neurological and Psychiatric Sciences, Florence, Italy

[8]Department of Medical Genetics, City of Hope Medical Center (Emeritus), Carlsbad Science Foundation, Monrovia, California

[9]Neurosciences Research Group, Institute of Genetics, School of Medicine, National University of Colombia, Bogota, Colombia

[10]Department of Public Health/Molecular Geriatrics, Uppsala University, Uppsala, Sweden

[11]Harvard Medical School, Massachusetts General Hospital, Charlestown, Massachusetts

[12]Choju Medical Institute, Fukushimura Hospital, Toyohashi, Aichi, Japan

[13]CNS Research Celera Diagnostics, Alameda, California

[14]Biology Department, Human Genome Research Center, Institute of Biosciences, University of São Paulo-IBUSP, São Paulo, Brazil

[15]Medical School, University of Tampere, Tampere, Finland

[16]Centre for Laboratory Medicine, Tampere University Hospital, Tampere, Finland

[17]Turku PET Centre, University of Turku, Turku, Finland

[18]Department of Mental Retardation and Birth Defect Research, National Institute of Neuroscience, National Center of Neurology and Psychiatry, Kodaira, Tokyo, Japan

[19]Department of Psychiatry, Institute of Clinical Medicine, University of Tsukuba, Tsukuba, Ibaraki, Japan

Received 3 December 2008; Accepted 15 April 2009

How to Cite this Article:
Fukumoto N, Fujii T, Combarros O, Kamboh MI, Tsai S-J, Matsushita S, Nacmias B, Comings DE, Arboleda H, Ingelsson M, Hyman BT, Akatsu H, Grupe A, Nishimura AL, Zatz M, Mattila KM, Rinne J, Goto Y, Asada T, Nakamura S, Kunugi H. 2010. Sexually Dimorphic Effect of the Val66Met Polymorphism of *BDNF* on Susceptibility to Alzheimer's Disease: New Data and Meta-Analysis.
Am J Med Genet Part B 153B:235–242.

Additional Supporting Information may be found in the online version of this article.
Grant sponsor: Health and Labor Sciences Research Grants; Grant sponsor: National Institute of Biomedical Innovation (NIBIO); Grant sponsor: Japan Society for the Promotion of Science (JSPS).
Noriko Fukumoto and Takashi Fujii contributed equally to this work.
Anges Lumi Nishimura's present address is Institute of Psychiatry, King's College London, MRC Centre for Neurodegenerative Research, Academic Neurology (PO43), De Crespigny Park, Denmark Hill, London, UK.
*Correspondence to:
Hiroshi Kunugi, M.D., Ph.D., Department of Mental Disorder Research, National Institute of Neuroscience, National Center of Neurology and Psychiatry, Kodaira, Tokyo 187-8502, Japan. E-mail: hkunugi@ncnp.go.jp
Published online 5 June 2009 in Wiley InterScience (www.interscience.wiley.com)
DOI 10.1002/ajmg.b.30986